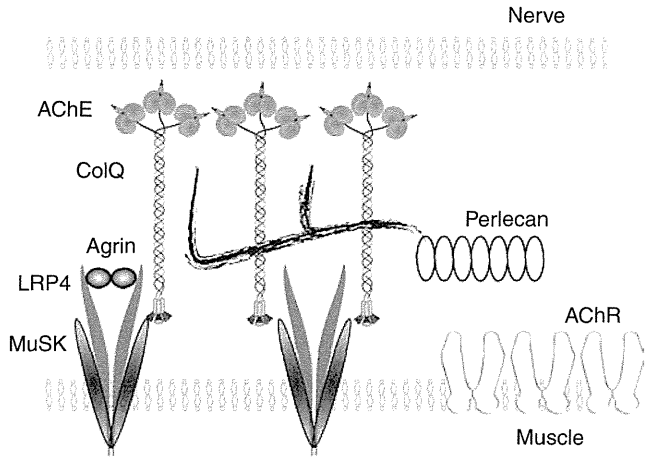

Figure 1 Schematic of anchoring of collagen Q (ColQ) to neuromuscular junction (NMJ). Twelve catalytic subunits of acetylcholinesterase (AChE) are attached to ColQ to form ColQ-tailed AChE. Two heparan sulfate proteoglycan-binding domains of ColQ are bound to perlecan. C-terminal domain of ColQ is bound to muscle-specific kinase (MuSK). Nerve-derived agrin binds to an LRP4–MuSK complex and induces rapsyn-mediated clustering of acetylcholine receptors (AChR) by phosphorylating AChR.

the present study open a new therapeutic avenue for treating many inherited defects of extracellular matrix proteins.

RESULTS

Intravenous administration of AAV8-*COLQ* normalizes motor functions of *Colq*$^{-/-}$ mice

We explored the recovery of the muscular phenotype of *Colq*$^{-/-}$ mice by viral delivery of a functional ColQ molecule. Therefore, we constructed a recombinant AAV serotype 8 carrying human *COLQ* cDNA. AAV serotype 8 (AAV8) is efficiently delivered to skeletal muscle after systemic injection.[16] We intravenously administered 1×10^{11}–2×10^{12} viral genome (vg) copies of AAV8-*COLQ* into 4-week-old *Colq*$^{-/-}$ mice. These mice exhibit muscle weakness, myasthenia, tremor, kyphosis, involuntary vocalization, and a slower growth rate than their wild-type littermates.[12] However, a single injection of 2×10^{12} vg, gradually improved their motor function to reach the level of that of wild type (**Figure 2a**). Furthermore, there were no signs of fatigue 6 weeks after the therapeutical injection (**Figure 2b**). Voluntary exercise in the treated mice also increased gradually but did not reach the level of wild type even at 5 weeks after injection (**Figure 2c**). The improved motor activities of treated mice are also demonstrated in **Supplementary Video 1**. Pairs of treated mice gave birth to *Colq*$^{-/-}$ pups and reared them to maturity. In longitudinal studies of three treated mice, all survived 18–20 months. Motor functions of the treated mice were declined at 48 weeks after injection but to the similar levels as those of wild type (**Figure 2a,c**). These observations clearly indicate the long-term therapeutic potential of a single viral injection of AAV.

AAV8-*COLQ* normalizes the neuromuscular synaptic transmission

To estimate recovery of neuromuscular transmission, we performed electrophysiological studies (**Table 1**). Treatment with

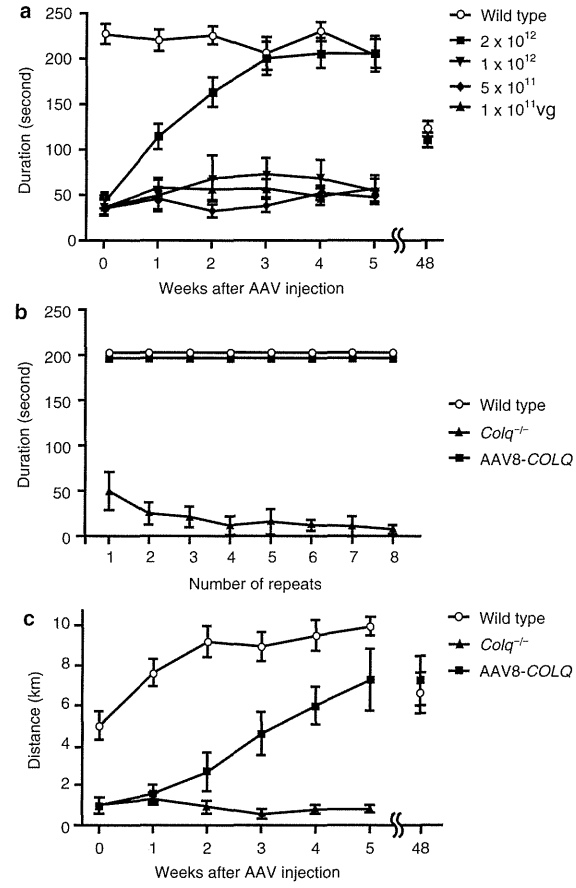

Figure 2 Exploration of motor function after intravenous injection of AAV8-*ColQ* to the tail vein of *Colq*$^{-/-}$ mice. (**a**) Motor function on the rotarod. The rotation was linearly accelerated from 0 to 40 r.p.m. in 240 seconds. Five groups of six mice were studied. Each group consisted of 4-week old mice and was either injected or not (control group) with increasing numbers of viral particles. Three weeks after their AAV8-*COLQ* injection, only the group of mice treated with 2×10^{12} vg remained on the rod as long as the wild-type littermates. Importantly, there was a progressive motor function recovery during the first 3 weeks after injection of *Colq*$^{-/-}$ mice. Symbols indicate mean and SE of six mice for each experiment. Mean and SE of the durations on the rotarod of two treated mice at 48 weeks after treatment is indicated along with that of the four age-matched wild-type mice. (**b**) Fatigue test using the rotarod was performed on three groups of a total of 18 mice. The rotation speed was fixed at 10 r.p.m. and the mice were immediately placed back on the rod each time they fell. Mice injected with 2×10^{12} vg exhibited no fatigue at 6 weeks after injection, whereas untreated *Colq*$^{-/-}$ mice fell increasingly more rapidly off the rod. (**c**) Voluntary movements were quantified by a counter-equipped running wheel. Plots show mean and SE of the number of rotations over 24 hours in each group of six mice (wild type, *Colq*$^{-/-}$, and AAV8-*COLQ*). Only the group of mice treated with 2×10^{12} vg increased the number of rotations every week but they did not reach the level of wild-type mice at 5 weeks after injection. Mean and SE of the number of rotations of two treated mice at 48 weeks after treatment is indicated along with that of the four age-matched wild-type mice. AAV8, adeno-associated virus serotype 8; ColQ, collagen Q.

AAV8-*COLQ* reduced decrements of the compound muscle action potentials in response to repetitive nerve stimulation at 2 Hz, reduced the amplitudes of miniature endplate potentials (MEPPs), shortened the miniature endplate potential decay time constants (**Figure 3**), and acquired responses to neostigmine. Endplate potential quantal content, which was decreased in

Table 1 Repetitive nerve stimulation and microelectrode studies

	Wild type	Wild type with neostigmine	*Colq*$^{-/-}$	*Colq*$^{-/-}$ with neostigmine	Treated *Colq*$^{-/-}$	Treated *Colq*$^{-/-}$ with neostigmine
Repetitive nerve stimulation[a]	0.92 ± 0.01* (2)	n.a.	0.58 ± 0.05 (3)	n.a.	0.76 ± 0.02* (3)	n.a.
EPP quantal content[b]	39.8 ± 2.3** (18)	n.a.	28.2 ± 1.8 (19)	n.a.	24.1 ± 1.6 (18)	n.a.
MEPP amplitude (mV)[c]	0.77 ± 0.04** (31)	1.52 ± 0.12 (18)	1.52 ± 0.11 (19)	1.52 ± 0.07 (10)	0.68 ± 0.02** (25)	0.98 ± 0.05** (24)
EPP amplitude (mV)[d]	30.6	n.a.	42.9	n.a.	16.4	n.a.
MEPP decay time (ms)[c]	1.77 ± 0.06** (31)	2.27 ± 0.08** (18)	3.07 ± 0.12 (19)	2.99 ± 0.09 (10)	2.45 ± 0.08** (25)	3.66 ± 0.09** (24)

Abbreviations: AChR, acetylcholine receptors; ColQ, collagen Q; EPP, endplate potential; MEPP, miniature endplate potential; n.a., not applicable.
Values represent mean ± SE. T = 29 ± 0.5 °C for EPP and MEPP recordings. Numbers in parenthesis indicate the number of recordings for repetitive nerve stimulation and the number of EPs from one or two mice for the other assays.
[a]Repetitive nerve stimulations were performed at 2 Hz, and the relative areas of compound muscle action potential (CMAP) of the fourth to the first stimulations are indicated. [b]Quantal content of EPP at 0.5 Hz stimulation corrected for resting membrane potential of –80 mV, nonlinear summation, and non-Poisson release. As the quantal contents of EPP are higher than 10, corrected values are indicated according to Cull-Candy *et al.*[45c] Normalized for resting membrane potential of –80 mV and a mean muscle fiber diameter of 55 µm. The actual fiber diameters were 45 ± 3.6 µm (mean ± SD, n = 31) for wild-type mice, 43 ± 3.0 µm (n = 19) for *Colq*$^{-/-}$ mice, and 46 ± 4.2 µm (n = 25) for the treated *Colq*$^{-/-}$ mice. [d]Estimated EPP amplitude is the product of the EPP quantal content and the MEPP amplitude. As AChR was partly blocked with curare for EPP recordings and not for MEPP recordings, we could not directly measure EPP amplitudes. Predicted low EPP amplitudes in treated mice suggest that the improvement of motor function was likely due to amelioration of depolarization block and/or of endplate myopathy.
*P < 0.05 and **P < 0.001 compared to *Colq*$^{-/-}$ mice by Student's t-test.

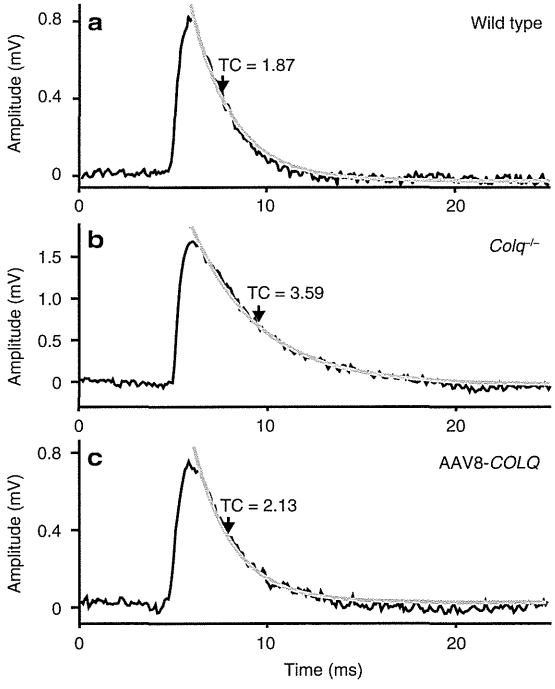

Figure 3 Representative miniature endplate potential (MEPP) recordings of diaphragm muscles of (a) wild type, (b) *Colq*$^{-/-}$, and (c) AAV8-*COLQ*-treated mice. (**b**) *Colq*$^{-/-}$ mice have higher MEPP amplitude and a longer decay time constant (TC) than (**a**) wild-type mice. AAV8-*COLQ* treatment shortened the decay TC and lowered the MEPP amplitude. Gray lines represent fitted exponential decay curves. AAV8, adeno-associated virus serotype 8; ColQ, collagen Q.

Colq$^{-/-}$ mice, was further decreased by the treatment, in contrast to our expectation.

Human ColQ-tailed AChE is anchored to the mouse NMJ *in vivo*

To further evaluate that the rescue was due to restitution of AChE at the NMJ, we used histological methods to visualize ColQ and AChE on muscle sections (**Figure 4a–c**). ColQ and AChE were colocalized to acetylcholine receptors (AChR) at the NMJ, confirming that ColQ-tailed AChE was specifically clustered to the target tissue. Although, we failed to observe improvement of motor functions with 1 × 10^{12} vg or less (**Figure 2a**), we still detected ColQ and AChE at NMJs with smaller amounts (data not shown). This suggests that a certain amount of viral genomes is required to exhibit improvement of motor deficits.

The ultrastructural morphology of treated mice also improved compared with age-matched *Colq*$^{-/-}$ mice (**Figure 4d–f**). The NMJ ultrastructures were variable from one to another in wild type, *Colq*$^{-/-}$, and treated mice, and we quantified the electron micrograph pictures (**Supplementary Table S1**). Quantitative analysis of presynaptic ultrastructures demonstrated that, in soleus slow-twitch muscle, Schwann cell invagination was mitigated, which increased the nerve terminal length, but the nerve terminal area remained essentially the same. Postsynaptic area and postsynaptic membrane length were also increased in soleus muscle of treated mice. In the extensor digitorum longus fast-twitch muscle, however, significant improvement was observed only in the ratio of enwrapped nerve terminal. Thus, the morphological improvements were more prominent in the soleus rather than in extensor digitorum longus muscles.

AAV8-*COLQ* restores the amount of ColQ-tailed AChE in the muscle to 89.3% of wild type

To estimate the efficiency of intravenous administration of AAV8-*COLQ*, we quantified the amount of the transduced *COLQ* mRNA, as well as ColQ-tailed AChE, in the muscle. We estimated the amount of *COLQ* mRNA in hindlimbs by a TaqMan probe, and found that the treated mice expressed the transduced *COLQ* at 92.5 ± 47.8% (mean ± SE, n = 4) of wild type. ColQ-tailed AChE from hindlimbs of the treated mice was fractionated by sucrose density-gradient ultracentrifugation. Sedimentation analysis revealed that AAV8-*COLQ* muscles have similar peaks of ColQ-tailed AChE species as those of wild type (**Figure 5a–c**). We also quantified the amount of globular AChE and ColQ-tailed AChE in gastrocnemius muscles of treated mice (**Figure 5d**). As previously reported, the amount of globular AChE was slightly lower in *Colq*$^{-/-}$ mice,[12] and this was normalized by treatment

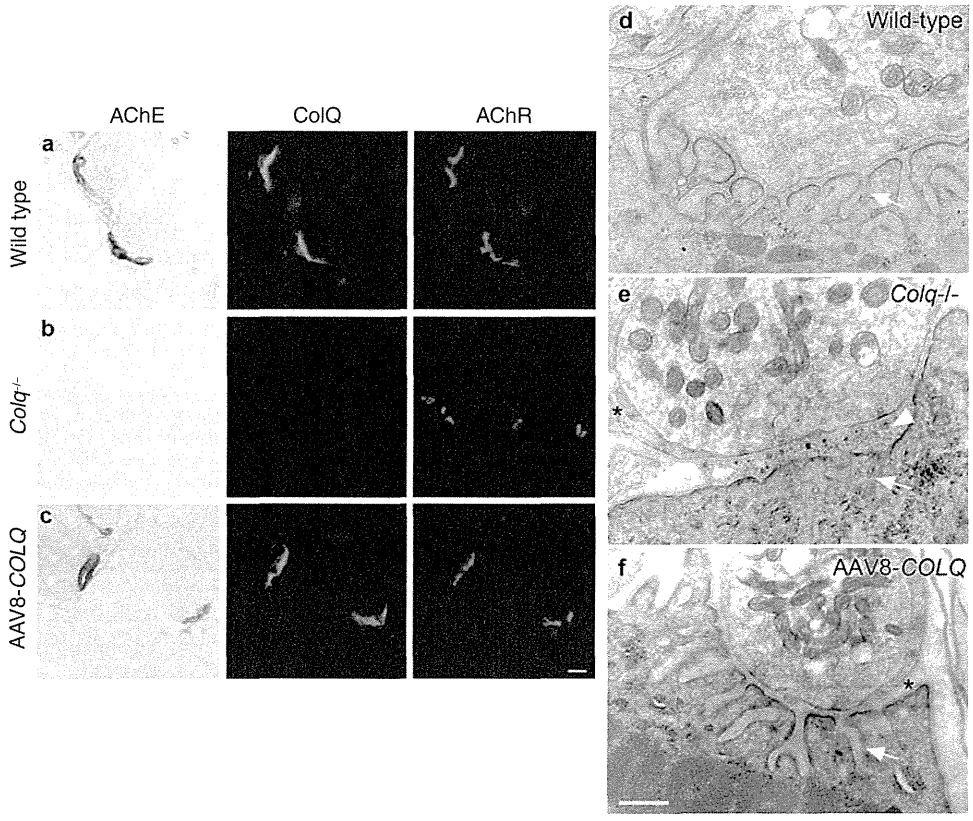

Figure 4 Histologies and ultrastructures of the neuromuscular junctions (NMJs). Localization of acetylcholinesterase (AChE) activity, collagen Q (ColQ), and acetylcholine receptors (AChR) in quadriceps muscles of (**a**) wild type, (**b**) *Colq*$^{-/-}$, and (**c**) AAV8-*COLQ* mice. Mice treated with 2 × 10^{12} vg of intravenous AAV8-*COLQ* express ColQ-tailed AChE at NMJ. AChE is stained for its activity. ColQ and AChR are detected by the polyclonal anti-ColQ antibody and α-bungarotoxin, respectively. Bar = 10 μm (**a–c**). Representative stainings of six mice in each group are indicated. Ultrastructures of soleus muscle NMJ (**d–f**). (**e**) *Colq*$^{-/-}$ mice show simplified synaptic clefts (arrow) and widening of the synaptic space (arrow head), whereas the NMJ ultrastructure of AAV8-*COLQ* mice (**f**) is indistinguishable from that of wild type (**d**). AAV8-*COLQ* mice still have small nerve terminals and invaginated Schwann cells (*). Bar = 1 μm (**d–f**). Representative ultrastructures of 27–41 electron micrograph (EM) pictures (see **Supplementary Table S1**) are indicated. AAV8, adeno-associated virus serotype 8.

with AAV8-*COLQ*. Treatment with AAV8-*COLQ* also restored ColQ-tailed AChE to 89.3 ± 9.6% (mean ± SD, $n = 4$) of wild type at 6 weeks after treatment. We also quantified ColQ-tailed AChE at 48 weeks after treatment and found that the amount was still 81.8 ± 21.6% (mean ± SD, $n = 2$) of the age-matched wild-type mice ($n = 3$). Although soleus slow-twitch muscle exhibited prominent improvement with the ultrastructural analysis, the available amount of soleus muscle was too small for the biochemical assay.

We also examined whether ColQ-tailed AChE was produced in the liver because AAV8 efficiently transduces hepatocytes.[15] AAV8-*COLQ* increased the *COLQ* mRNA level in the liver from 3.4 ± 0.34% (mean ± SE of five wild-type mice) to 61.3 ± 12.6% (mean ± SE of five treated mice) compared to those in the muscle of wild-type mice ($n = 5$). The *Ache* mRNA levels in the liver of wild type, *Colq*$^{-/-}$, and treated mice, however, were estimated to be <0.5% of that in wild-type muscle. The *Ache* mRNA levels in the liver were too low to be accurately quantified by real-time reverse transcription-PCR. Sedimentation profiles revealed no peaks of ColQ-tailed AChE in the liver of either wild type, *Colq*$^{-/-}$, or treated mice (**Supplementary Figure S1a–c**). This was probably due to lack of *Ache* expression. Globular AChE species observed in the sedimentation analysis was likely to represent AChE on the erythrocyte cell membrane.[17] These data suggest that AAV8-*COLQ* did not induce expression of ColQ-tailed AChE in the liver.

Local intramuscular injection of AAV8-*COLQ* expresses ColQ-tailed AChE at NMJs of noninjected limbs

Prominent improvements that we observed in AAV8-*COLQ*-treated mice raised a possibility that ColQ-tailed AChE moved from the transduced muscle cells to other muscle cells. We thus tested this possibility in the following experiments.

First, we have previously reported that the human recombinant ColQ-tailed AChE can be anchored to the synaptic basal lamina of the frog NMJ.[18] We tested this anchoring using mouse NMJs. We purified ColQ-tailed AChE expressed in HEK293 cells and incubated this with a section of skeletal muscle from *Colq*$^{-/-}$ mice. As expected, ColQ and AChE were detected at the mouse NMJ (**Supplementary Figure S2**), which supports the notion that ColQ-tailed AChE can be moved and anchored to the target *in vitro*.

Next, we tested whether ColQ-tailed AChE moved from the transduced muscles to the nontransduced muscles. We injected AAV8-*COLQ* to the left anterior tibial muscle. As expected, AChE and ColQ were rescued at the NMJs of the injected muscle. In addition, AChE and ColQ were also detected at all the examined

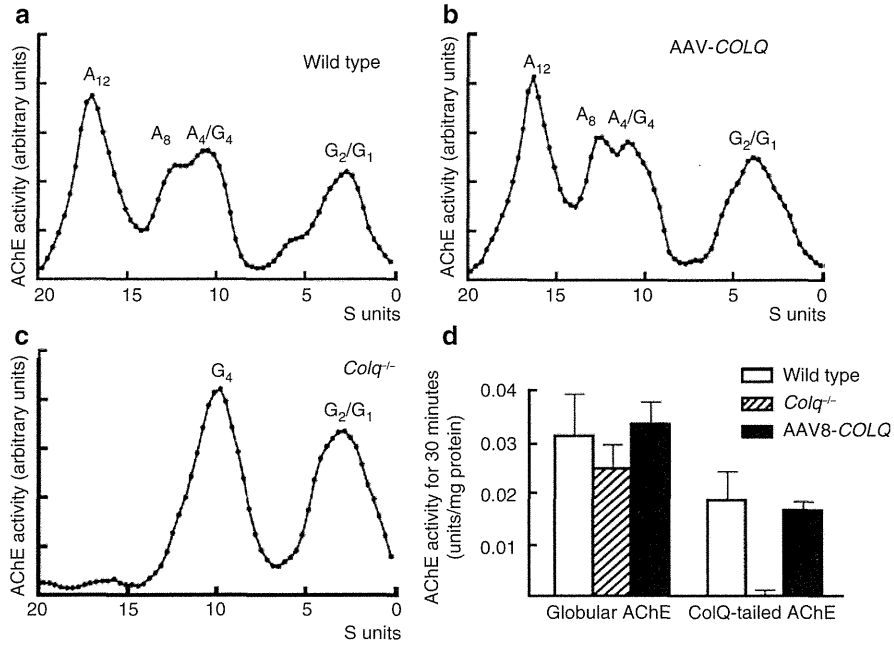

Figure 5 Quantification and biochemical analysis of acetylcholinesterase (AChE) recovery in muscles. Intravenous injection of 2×10^{12} vg of AAV8-*COLQ* into (**b**) *Colq*$^{-/-}$ mice gives rise to a sedimentation profile that is identical to that of (**a**) wild type, whereas (**c**) *Colq*$^{-/-}$ mice carry no collagen Q (ColQ)-tailed AChE. A_4, A_8, and A_{12} species carry 4, 8, and 12 AChE catalytic subunits attached to a triple helical ColQ. G_1, G_2, and G_4 species carry 1, 2, and 4 AChE catalytic subunits but without ColQ. A representative profile of three experiments is indicated. (**d**) Quantification of globular and ColQ-tailed AChE species (mean and SD, $n = 4$). The activity of ColQ-tailed AChE in the skeletal muscle of AAV8-*COLQ* mice is restored to 89 ± 10% of that of wild type. AAV8, adeno-associated virus serotype 8.

NMJs in noninjected muscles (data not shown). These results, however, could not exclude the possibility that AAV8-*COLQ* had been delivered to noninjected muscles in the form of a virus.

Local intramuscular injection of AAV1-*COLQ-IRES-EGFP* expresses ColQ-tailed AChE at NMJs of noninjected limbs

To reduce systemic delivery of AAV8 and to identify infected cells, we packed *COLQ* cDNA into the AAV serotype 1 (AAV1) that is known to transduce the injected muscle fibers locally.[19] In addition, we fused *COLQ* and internal ribosome entry site (*IRES*)-*EGFP* to express green fluorescent protein (GFP) in transduced cells synthesizing ColQ. We injected 2×10^{11} vg of AAV1-*COLQ-IRES-EGFP* into the left anterior tibial muscle of *Colq*$^{-/-}$ mice, while blocking the blood flow with a tourniquet for 20 minutes to restrict the distribution of the virus. The transduction efficiencies of AAV1-*COLQ-IRES-EGFP* were as follows: left anterior tibial muscle, 1.70 ± 0.29 viral copies per nucleus; right gastrocnemius muscle, 0.00100 ± 0.00079 copies; and bilateral brachial muscles, 0.00126 ± 0.00058 copies (mean ± SD, $n = 3$). Although only a fraction of the injected AAV1-*COLQ-IRES-EGFP* moved to noninjected limbs, we observed colocalization of ColQ and AChE at all the examined NMJs of right gastrocnemius, right tibialis anterior, both triceps, and both biceps in four examined mice (Figure 6a). We analyzed a total of 200–400 NMJs per muscle. In contrast, expression of intracellular enhanced GFP (EGFP) was not observed in noninjected limb muscles. We also quantified ColQ-tailed AChE in the noninjected bilateral forelimbs and right hindlimb, and found that the amounts were 21.5 ± 10.2% and 28.4 ± 10.0% (mean ± SD, $n = 4$), respectively, of those of wild type (Figure 6b).

ColQ-tailed AChE protein reaches and binds to remote NMJs

The presence of ColQ in noninjected muscles strongly suggests that the ColQ-tailed AChE is assembled intracellularly in one muscle and has moved to noninjected muscles, where it is anchored to the NMJs. To directly test this possibility, the gluteus maximus muscles of 5-week-old *Colq*$^{-/-}$ mice ($n = 4$) were injected daily with 2 μg of recombinant human ColQ-tailed AChE for 7 days. Histological analysis revealed the presence of ColQ and AChE in all of the examined NMJs from triceps muscles (Figure 7a). Quantitative analysis of ColQ signal intensities at the NMJs of noninjected triceps demonstrated that the ColQ-positive areas normalized for the AChR-positive area per NMJ became indistinguishable from that of wild type (Figure 7b). Furthermore, the ColQ signal intensity normalized for the AChR area per NMJs reached ~41.6% of that of wild type (Figure 7c). The *Colq*$^{-/-}$ mice could not hang on the wire at all, but the protein-injected mice acquired the ability to hang on the wire for two or more minutes from the fourth day of injection.

DISCUSSION

Effective and persistent gene therapy of ColQ with a single intravenous injection of AAV8-*COLQ*

We present an efficient and persistent recovery of AChE at the NMJ after a single intravenous administration of AAV8-*COLQ* in a *Colq*$^{-/-}$ mouse model of congenital myasthenic syndrome

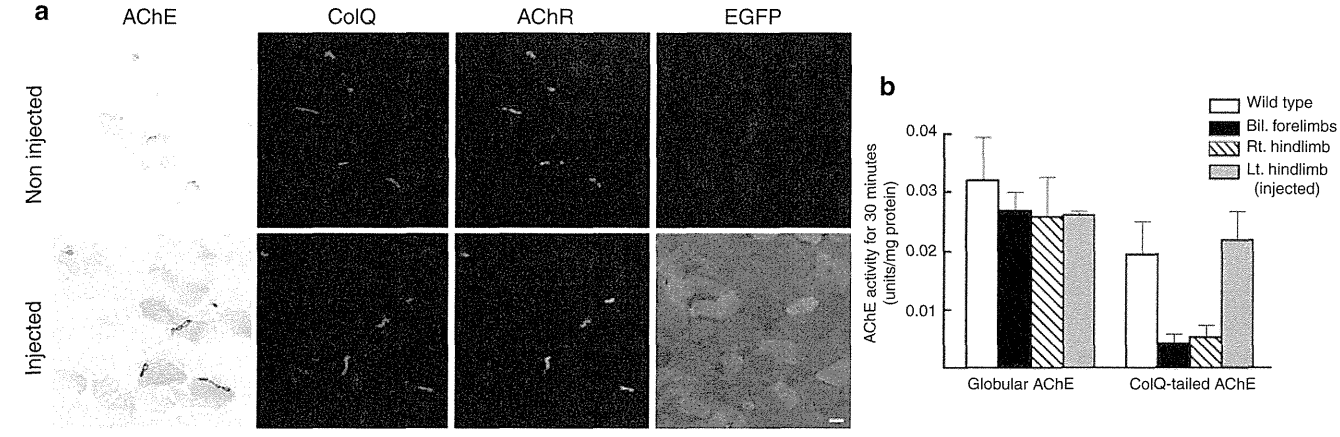

Figure 6 Intramuscular injection of 2×10^{11} vg of AAV1-*COLQ-IRES-EGFP* into the left anterior tibial muscle of *Colq*$^{-/-}$ mice. (**a**) Acetylcholinesterase (AChE) activity and collagen Q (ColQ) are colocalized to the acetylcholine receptors (AChR) in the injected muscle, as well as in the noninjected triceps muscle, although the signal intensities are not as high as those of the injected muscle. In contrast to ColQ, an intracellular molecule, enhanced green fluorescent protein (EGFP), is expressed only in the injected muscle, but not in the noninjected muscle. Bar = 10 μm. (**b**) Quantification of globular and ColQ-tailed AChE species of skeletal muscles (mean and SD, $n = 4$). In the injected left hindlimb, the activity of ColQ-tailed AChE is similar to that of wild type. In the noninjected both forelimbs and right hindlimb, the activities are 21.5 and 28.4% of wild type, respectively. AAV1, adeno-associated virus serotype 1.

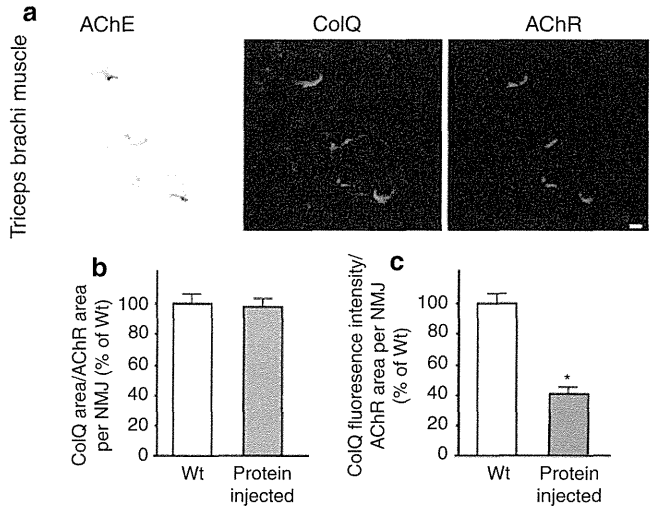

Figure 7 Injection of purified recombinant human collagen Q (ColQ)-tailed acetylcholinesterase (AChE). (**a**) Daily injection of 0.2 μg human recombinant ColQ-tailed AChE into the gluteus maximus muscles of *Colq*$^{-/-}$ mice rescues AChE activity and ColQ in the noninjected triceps where they are colocalized to acetylcholine receptors (AChR). Bar = 10 μm. (**b**) The size of ColQ-positive area is normalized for the size of AChR-positive area at the neuromuscular junctions (NMJs) of noninjected triceps. (**c**) Signal intensities of ColQ at the NMJs of noninjected triceps. Mean and SE are indicated. WT, wild-type mice, number of NMJs = 43; Protein injected, mice injected with ColQ-tailed AChE, number of NMJs = 42. *$P < 0.001$. Signal intensities are normalized to that of *Colq*$^{-/-}$ mice. Quantitative analyses were performed with the BZ-9000 microscope and the Dynamic Cell Count software BZ-H1C (Keyence).

with deficit in AChE. We observed ColQ-tailed AChE at all of the NMJs examined and the amount of the anchored AChE reached 89.3% of the wild-type level. The improved motor functions lasted at least 48 weeks after treatment and the treated mice survived 18–20 months, which is in contrast to at most 6-month lifespan of *Colq*$^{-/-}$ mice.[12] Although >99.5% of the vector genome stays episomal in mouse muscles even at 57 weeks after injection,[20,21] expression of the transgene in skeletal muscle lasts for 1.0–1.5 years without a decline in immunocompetent mice.[22,23] Our studies also underscore the long-lasting expression of the transgene delivered by AAV.

Rat *Colq*[24] and human *COLQ*[7] have two distinct promoters and generate ColQ1 and ColQ1a transcripts, which respectively include exon 1 and exon 1a and encode distinct signal peptides. A nerve-derived factor, calcitonin gene-related peptide, controls the expression of ColQ1a at the NMJs of fast-twitch muscles. However, in slow-twitch muscles, expression of ColQ1 occurs throughout the muscle fibers and is controlled by Ca^{2+}/calmodulin-dependent protein kinase II and myocyte enhancer factor 2.[24,25] As our viral construct was driven by the cytomegalovirus promoter, spatial and temporal regulation of ColQ expression should have been lost. In addition, our construct expressed ColQ1 and not ColQ1a, which was expected to be physiological for slow-twitch muscle but not for fast-twitch muscles. The prominent ultrastructural improvement in slow-twitch muscles rather than fast-twitch muscles may be partly because AAV8-*COLQ* encodes ColQ1 and not ColQ1a. This also suggests that the N-termini of ColQ1 and 1a have different functions. The pattern of ColQ expression resulting from our strategy was not physiological in three ways: (i) lack of subsynaptic nuclei-specific expression of ColQ, (ii) a ubiquitous cytomegalovirus promoter, and (iii) the exclusive expression of ColQ1. Despite these features, the motor and the synaptic functions are improved; AChE is locally accumulated at the NMJ in our treated mice. This suggests that the precise genetic control of the expression of ColQ is not the key factor for clustering of AChE and tissue-targeting signals of ColQ are sufficient to functionally restore AChE at the NMJ.

The protein-anchoring therapy

Although ColQ-tailed AChE in the serum of either wild type, *Colq*$^{-/-}$, or treated mice was less than a detection threshold in the

sedimentation analysis (**Supplementary Figure S1d–f**), anchoring of ColQ-tailed AChE to remote NMJs was supported by two lines of evidence: local intramuscular injections of AAV1-*COLQ-IRES-EGFP* (Figure 6) and of the purified recombinant ColQ-tailed AChE protein complex (Figure 7). In either case, AChE at the NMJ of the noninjected muscle originates from ColQ-tailed AChE arising from another source; not from local secretion and retention of ColQ-tailed AChE synthesized by subsynaptic nuclei followed by assembly and maturation in the postsynaptic area as in wild-type mice. The overlay of recombinant ColQ-tailed AChE *in vitro* either on normal muscle tissue sections of frog[5,18] or of *Colq*$^{-/-}$ mouse (**Supplementary Figure S2**) demonstrates that ColQ harbors a signal that targets AChE to the NMJ. The dual interactions of ColQ with MuSK[6] and perlecan,[5] which are both required in the overlay experiment,[18] are likely to restrict ColQ to the NMJ. In endplate AChE deficiency, point mutations that affect the binding of ColQ to MuSK prevent the accumulation of AChE.[18] Although no mutation has been reported at the heparan sulfate proteoglycan-binding domains of ColQ in endplate AChE deficiency, the reduction of perlecan mimicking Schwartz–Jampel syndrome reduces the level of AChE and ColQ at the NMJ.[26,27] All of these observations suggest that the combination of MuSK and perlecan determines the number of ColQ-tailed AChE anchored at the NMJ. This notion was previously termed as "molecular parking lots" by Rotundo and colleagues.[28]

ColQ-tailed AChE is a nanostructure made of a rigid collagen of 50-nm length and three AChE tetramers. ColQ-tailed AChE is apparently able to move from one muscle to another as demonstrated by clustering in the triceps muscle after protein injection into the gluteus. A similar approach is inherently employed by nature, as exemplified by fibronectin that is ubiquitously present in extracellular matrices and is largely derived from liver.[29] Injection of a protein complex is reported with laminin-111.[30] An intramuscularly or intraperitoneally injected laminin-111 is distributed to the basal lamina of skeletal and cardiac muscles in an mdx-mouse model of Duchenne muscular dystrophy. In contrast to our strategy, laminin-111 is not expressed or accumulated in normal or dystrophic adult muscles. Their studies exploit an ectopic deposition of laminin-111 to induce expression of α_7-integrin that stabilizes the sarcolemma of dystrophic muscle fibers.

The ColQ must be synthesized in cells that produce a splice variant T of AChE for obtaining the correct assembly of the complex.[2] A single muscle fiber harbors hundreds of nuclei that are functionally compartmentalized, and a molecule expressed in a single nucleus goes through the muscle fiber only for a short distance.[31,32] Thus, the multinucleation of muscle fibers is unlikely to have contributed to the restoration of function in the *Colq*$^{-/-}$ mice of our study. Similar specific clustering of a muscle-generated protein to the NMJ has been reported with laminin β2.[33] When laminin β2 is expressed throughout muscle fibers by the MCK promoter in transgenic mice, it is clustered at the NMJ.

The inability to achieve efficient and specific delivery of a transgene to the target tissue often prevents the application of gene therapy to model animals and patients.[34] Here, we propose the protein-anchoring strategy that provides a new therapeutic approach for congenital defects of extracellular matrix proteins.[35] The potential candidate molecules of the protein-anchoring therapy include laminin α2 causing laminin-α2-deficient congenital muscular dystrophy,[36] perlecan causing Schwartz–Jampel syndrome,[26,37] and collagen VI causing Ullrich syndrome.[38] It should be emphasized that this strategy can be potentially used for a huge number of diseases caused by mutations of genes encoding proteins of the extracellular matrices in general.

MATERIALS AND METHODS

Preparation of AAV carrying COLQ. Human *COLQ* cDNA[7] was cloned into pAAV-MCS (AAV Helper-Free system; Stratagene, Santa Clara, CA) that carries the cytomegalovirus promoter to obtain a pAAV-*COLQ*. We also inserted *IRES-EGFP* to make pAAV-*COLQ-IRES-EGFP*. To make AAV8-*COLQ*, HEK293 cells were cotransfected with the following plasmids: the proviral vector plasmid pAAV-*COLQ*, the AAV8 chimeric helper plasmid pRC8, and the adenoviral helper plasmid pHelper (Stratagene) using calcium phosphate coprecipitation method.[39] To make AAV1-*COLQ-IRES-EGFP*, we transfected HEK293 cells with pAAV-*COLQ-IRES-EGFP*, the AAV1 chimeric helper plasmid pRep2Cap1, and pHelper. The AAV particles were concentrated by CsCl gradient ultracentrifugation for 3 hours[40] and further purified with the quick dual ion-exchange procedures.[41] The viral titer was estimated by quantitative PCR in real-time using MX3000p (Stratagene).[42]

Administration of AAV carrying COLQ to Colq$^{-/-}$ mice. All animal studies were approved by the Animal Care and Use Committee of the Nagoya University Graduate School of Medicine. For intravenous administration, 1×10^{11}–2×10^{12} vg of AAV8-*COLQ* were injected into the tail vein of 4-week-old *Colq*$^{-/-}$ mice.[12] For intramuscular administration, 2×10^{11} vg of AAV1-*COLQ-IRES-EGFP* were injected into the left anterior tibial muscle of 4-week-old *Colq*$^{-/-}$ mice. The left proximal thigh was tightly ligated with a tourniquet for 20 minutes during intramuscular injection to prevent vascular delivery of viral particles throughout the body.

Motor activity tests. Muscle weakness and fatigability were measured with a rotarod apparatus (Ugo, Basile, Italy). Mice were first trained three times to be accommodated to the task. Mice were consecutively examined three times and were allowed to take a rest for 1 hour between individual tasks.

Running-wheel activity was used to quantify voluntary exercises. Each mouse was placed in a standard cage equipped with a counter-equipped running wheel (diameter, 14.7 cm, width, 5.2 cm; Ohara Medical, Tokyo, Japan). The running distances were recorded using the counter every 24 hours.

Histology. We raised a polyclonal ColQ antibody by injecting a synthetic peptide of SAALPSLDQKKRGGHKAC, corresponding to codons 34–51 in human ColQ, into rabbits. We confirmed that the raised antibody recognized ColQ by western blotting (**Supplementary Figure S3**) and that no signal was present in a section of *Colq*$^{-/-}$ mice (**Figure 4b** and **Supplementary Figure S2**). Mice were sacrificed at 6 weeks after treatment. Skeletal muscles of mice were frozen in the liquid nitrogen-cooled isopentane and sectioned at 8-μm thick with a Leica CW3050-4 cryostat at −20 °C. Muscle sections were blocked with 5% horse serum in phosphate-buffered saline for 20 minutes and incubated with the primary antibody (1:100) for 2 hours. Sections were then incubated with a secondary antibody (1:100) for 1 hour, along with Alexa-594-conjugated α-bungarotoxin (2.5 μg/ml) (Sigma, St Louis, MO) for visualizing AChR. Anti-rabbit and anti-mouse secondary antibodies were both FITC-labeled (Vector Lab, Burlingame, CA). For AAV1-*COLQ-IRES-EGFP*, we detected ColQ using anti-rabbit secondary antibody labeled with rhodamine (1:40; Santa Cruz, Santa Cruz, CA) and localized AChR by Alexa-647-conjugated α-bungarotoxin (2.5 μg/ml; Sigma). Signals of ColQ, AChE, AChR, and EGFP were examined with BX60 (Olympus, Tokyo, Japan) or BZ-9000 (Keyence, Osaka, Japan).

Mouse AChE activity was detected by the histochemical method at 6 weeks after treatment. Muscle sections were incubated for 20 minutes at 37 °C in the reaction mixture containing 1.73 mmol/l acetylthiocholine iodide, 38 mmol/l sodium acetate, 51 mmol/l acetic acid, 6 mmol/l sodium

citrate, 4.7 mmol/l copper sulfate, 0.5 mmol/l potassium ferricyanide, and 5×10^{-5} mol/l ethopropazine (Sigma), which is an inhibitor of butyrylcholinesterase.

Sedimentation biochemical analyses. Mice were sacrificed at 6 weeks after treatment. Sedimentation analysis was performed as previously described.[7] Proteins were extracted from the muscle and liver in a detergent buffer [10 mmol/l HEPES (pH 7.2), 1% CHAPS, 10 mmol/l EDTA, 2 mmol/l benzamidine, leupeptin (20 μg/ml) and pepstatin (10 μg/ml)] containing 0.8 mol/l NaCl. The eluate was applied on a 5–20% sucrose density gradient, which was made in the detergent buffer containing 0.8 mol/l NaCl, along with β-galactosidase (16S) and alkaline phosphatase (6.1S) as internal sedimentation standards. Centrifugation was performed in a Beckman SW41Ti rotor at 4 °C for 21 hours at 38,000 r.p.m. AChE activity was assayed by the colorimetric method of Ellman in the presence of 5×10^{-5} mol/l ethopropazine.

For biochemical analysis, skeletal muscle was shattered by the Cool Mill (Toyobo, Osaka, Japan) in liquid nitrogen. We extracted globular forms of AChE into the NaCl-free detergent buffer, and ColQ-tailed AChE into detergent buffer containing 0.8 mol/l NaCl as previously described.[12] AChE activity was assayed using AChE-Specific Assay kit (Dojindo, Kumamoto, Japan) or the Ellman method and normalized by Torpedo AChE activity (Sigma).

Microelectrode studies. Phrenic nerve-diaphragm preparations were obtained from three wild type, three *Colq*$^{-/-}$, and three AAV8-*COLQ*-treated mice at 8 weeks of age, which corresponds to 4 weeks after treatment. We stimulated the sciatic nerve at 2 Hz and recorded compound muscle action potentials of gastrocnemius muscles using a needle electrode under deep anesthesia. For technical reasons, we could not analyze the limb muscles that we used in the other assays. After mice were sacrificed, miniature endplate potentials and evoked EPPs were recorded as described elsewhere.[43] Neostigmine methylsulfate (Elkins-Sinn, Cherry Hill, NJ) was used at a concentration of 10^{-6} g/ml in the bath to block cholinesterases. We employed the AxoGraph × 1.1.6 (AxoGraph Scientific, Sydney, Australia) for data analysis.

Electron microscopy. For electron microscopy, extensor digitorum longus and soleus muscles were fixed in ice-cold 3% glutaraldehyde buffered with 0.1 mol/l cacodylate buffer (pH 7.3) at 4 weeks after treatment. The endplate-rich region of the muscle was refixed in 2% OsO_4 in cacodylate buffer, dehydrated, and embedded in Epon812.

All thin sections were cut transversely, stained with lead citrate, and photographed in a JEM 1,200 EX electron microscopy. Morphometric analysis of the motor endplate was performed following the procedure of Engel and Santa,[44] and included the following: (i) presynaptic membrane length, in μm; (ii) nerve terminal area, in μm^2; (iii) number of synaptic vesicles per unit area, in numbers per μm^2; (iv) length of processes of Schwann cells on presynaptic membrane, in μm; (v) percentage of totally enwrapped nerve terminal by processes of Schwann cells; (vi) postsynaptic area of folds and clefts associated with a given nerve terminal, in μm^2; (vii) postsynaptic membrane length associated with a given nerve terminal, in μm; (viii) postsynaptic membrane length per unit postsynaptic area (postsynaptic membrane density), derived by dividing the value of (vii) by that of (vi), in μm per μm^2; (ix) postsynaptic to presynaptic membrane ratio. Endplates were localized and analyzed by established methods, and peroxidase-labeled α-bungarotoxin was used for the ultrastructural localization of AChR.[45] The images were quantified using the NIH Image 1.62 software (National Institutes of Health).

Expression and purification of recombinant ColQ. The plasmids that previously introduced human *COLQ* and human *ACHE* cDNAs into a pTargeT (Promega, Madison, WI)[7] were cotransfected into HEK293 cells. Proteins were extracted from the cells in Tris–HCl buffer [50 mmol/l Tris–HCl (pH 7.0), 0.5% Triton X-100, 0.2 mmol/l EDTA, leupeptin (2 μg/ml), and pepstatin (1 μg/ml)] containing 1 mol/l NaCl. The extracts were loaded onto HiTrap Heparin HP columns (GE Healthcare, Buckinghamshire, UK). The concentration of purified recombinant ColQ-tailed AChE was equivalent to ~4 μg/ml Torpedo AChE. We injected 50 μl of the purified ColQ-tailed AChE in phosphate-buffered saline daily into the gluteus maximus muscles of 5-week-old *Colq*$^{-/-}$ mice for a week. Mice were given a single intraperitoneal injection of 300 mg/kg cyclophosphamide monohydrate (10 mg/ml in saline) at 24 hours after the first ColQ-tailed AChE injection to suppress immunoreaction against the recombinant human protein.[46] After 7 days, mice were sacrificed and brachial muscles were stained for ColQ molecule and AChE activity as described above.

Real-time PCR/reverse transcription-PCR. For expression analysis, total RNAs from skeletal muscle and liver cells were extracted using the RNeasy Mini kit (Qiagen, Hilden, Germany) with *DNase*I and proteinase K treatment according to the manufacturer's instructions. First-stranded cDNA was synthesized using the ReverTra Ace reverse transcriptase (Toyobo). Expressions of human *COLQ*, mouse *Colq*, and mouse *Ache* were analyzed using the TaqMan (Applied Biosystems, Foster city, CA) probes and primers in LightCycler 480 (Roche, Mannheim, Germany). We also quantified 18S rRNA for normalization.

To quantify the transduction efficiency, total DNA was extracted from skeletal muscle and liver using the QIAamp DNA Mini Kit (Qiagen). The amount of viral genome was quantified by real-time PCR using a TaqMan probe targeting to human *COLQ*, as well as to mouse *Tert* encoding telomerase reverse transcriptase to normalize for the cell numbers.

SUPPLEMENTARY MATERIAL

Figure S1. Sedimentation analyses of AChE in the liver and serum.
Figure S2. Binding of human ColQ-tailed AChE proteins to the NMJ in muscle section of *Colq*$^{-/-}$ mice.
Figure S3. Western blot of a newly raised rabbit polyclonal anti-ColQ antibody (1:1,000).
Table S1. Morphometric analysis of endplate ultrastructures.
Video 1. First part: Two *Colq*$^{-/-}$ mice treated with an intravenous administration of 2×10^{12} vg of AAV8-*COLQ* (right cage) move around actively.

ACKNOWLEDGMENTS

We thank James M. Wilson for providing the chimeric helper plasmid pRC8 (identical to p5E18-VD2/8) and pRep2Cap1 (identical to p5E18RXCl). This work was supported by Grants-in-Aid from the Ministry of Education, Culture, Sports, Science, and Technology of Japan, and the Ministry of Health, Labor, and Welfare of Japan, as well as by Grant from ANR maladies rares. The authors declared no conflict of interest.

REFERENCES

1. Krejci, E, Thomine, S, Boschetti, N, Legay, C, Sketelj, J and Massoulié, J (1997). The mammalian gene of acetylcholinesterase-associated collagen. *J Biol Chem* **272**: 22840–22847.
2. Rotundo, RL (1984). Asymmetric acetylcholinesterase is assembled in the Golgi apparatus. *Proc Natl Acad Sci USA* **81**: 479–483.
3. Ruiz, CA and Rotundo, RL (2009). Limiting role of protein disulfide isomerase in the expression of collagen-tailed acetylcholinesterase forms in muscle. *J Biol Chem* **284**: 31753–31763.
4. Deprez, P, Inestrosa, NC and Krejci, E (2003). Two different heparin-binding domains in the triple-helical domain of ColQ, the collagen tail subunit of synaptic acetylcholinesterase. *J Biol Chem* **278**: 23233–23242.
5. Peng, HB, Xie, H, Rossi, SG and Rotundo, RL (1999). Acetylcholinesterase clustering at the neuromuscular junction involves perlecan and dystroglycan. *J Cell Biol* **145**: 911–921.
6. Cartaud, A, Strochlic, L, Guerra, M, Blanchard, B, Lambergeon, M, Krejci, E *et al.* (2004). MuSK is required for anchoring acetylcholinesterase at the neuromuscular junction. *J Cell Biol* **165**: 505–515.
7. Ohno, K, Brengman, J, Tsujino, A and Engel, AG (1998). Human endplate acetylcholinesterase deficiency caused by mutations in the collagen-like tail subunit (ColQ) of the asymmetric enzyme. *Proc Natl Acad Sci USA* **95**: 9654–9659.
8. Donger, C, Krejci, E, Serradell, AP, Eymard, B, Bon, S, Nicole, S *et al.* (1998). Mutation in the human acetylcholinesterase-associated collagen gene, COLQ, is responsible

for congenital myasthenic syndrome with end-plate acetylcholinesterase deficiency (Type Ic). *Am J Hum Genet* **63**: 967–975.
9. Ohno, K, Engel, AG, Brengman, JM, Shen, XM, Heidenreich, F, Vincent, A *et al.* (2000). The spectrum of mutations causing end-plate acetylcholinesterase deficiency. *Ann Neurol* **47**: 162–170.
10. Bestue-Cardiel, M, Sáenz de Cabezón-Alvarez, A, Capablo-Liesa, JL, López-Pisón, J, Peña-Segura, JL, Martin-Martinez, J *et al.* (2005). Congenital endplate acetylcholinesterase deficiency responsive to ephedrine. *Neurology* **65**: 144–146.
11. Mihaylova, V, Müller, JS, Vilchez, JJ, Salih, MA, Kabiraj, MM, D'Amico, A *et al.* (2008). Clinical and molecular genetic findings in COLQ-mutant congenital myasthenic syndromes. *Brain* **131**(Pt 3): 747–759.
12. Feng, G, Krejci, E, Molgo, J, Cunningham, JM, Massoulié, J and Sanes, JR (1999). Genetic analysis of collagen Q: roles in acetylcholinesterase and butyrylcholinesterase assembly and in synaptic structure and function. *J Cell Biol* **144**: 1349–1360.
13. Lee, HH, Choi, RC, Ting, AK, Siow, NL, Jiang, JX, Massoulié, J *et al.* (2004). Transcriptional regulation of acetylcholinesterase-associated collagen ColQ: differential expression in fast and slow twitch muscle fibers is driven by distinct promoters. *J Biol Chem* **279**: 27098–27107.
14. Ruiz, CA and Rotundo, RL (2009). Dissociation of transcription, translation, and assembly of collagen-tailed acetylcholinesterase in skeletal muscle. *J Biol Chem* **284**: 21488–21495.
15. Inagaki, K, Fuess, S, Storm, TA, Gibson, GA, Mctiernan, CF, Kay, MA *et al.* (2006). Robust systemic transduction with AAV9 vectors in mice: efficient global cardiac gene transfer superior to that of AAV8. *Mol Ther* **14**: 45–53.
16. Nakai, H, Fuess, S, Storm, TA, Muramatsu, S, Nara, Y and Kay, MA (2005). Unrestricted hepatocyte transduction with adeno-associated virus serotype 8 vectors in mice. *J Virol* **79**: 214–224.
17. Bouma, SR, Drislane, FW and Huestis, WH (1977). Selective extraction of membrane-bound proteins by phospholipid vesicles. *J Biol Chem* **252**: 6759–6763.
18. Kimbell, LM, Ohno, K, Engel, AG and Rotundo, RL (2004). C-terminal and heparin-binding domains of collagenic tail subunit are both essential for anchoring acetylcholinesterase at the synapse. *J Biol Chem* **279**: 10997–11005.
19. Wang, Z, Zhu, T, Qiao, C, Zhou, L, Wang, B, Zhang, J *et al.* (2005). Adeno-associated virus serotype 8 efficiently delivers genes to muscle and heart. *Nat Biotechnol* **23**: 321–328.
20. Schnepp, BC, Clark, KR, Klemanski, DL, Pacak, CA and Johnson, PR (2003). Genetic fate of recombinant adeno-associated virus vector genomes in muscle. *J Virol* **77**: 3495–3504.
21. Kay, MA (2007). AAV vectors and tumorigenicity. *Nat Biotechnol* **25**: 1111–1113.
22. Xiao, X, Li, J and Samulski, RJ (1996). Efficient long-term gene transfer into muscle tissue of immunocompetent mice by adeno-associated virus vector. *J Virol* **70**: 8098–8108.
23. Rivière, C, Danos, O and Douar, AM (2006). Long-term expression and repeated administration of AAV type 1, 2 and 5 vectors in skeletal muscle of immunocompetent adult mice. *Gene Ther* **13**: 1300–1308.
24. Krejci, E, Legay, C, Thomine, S, Sketelj, J and Massoulié, J (1999). Differences in expression of acetylcholinesterase and collagen Q control the distribution and oligomerization of the collagen-tailed forms in fast and slow muscles. *J Neurosci* **19**: 10672–10679.
25. Lau, FT, Choi, RC, Xie, HQ, Leung, KW, Chen, VP, Zhu, JT *et al.* (2008). Myocyte enhancer factor 2 mediates acetylcholine-induced expression of acetylcholinesterase-associated collagen ColQ in cultured myotubes. *Mol Cell Neurosci* **39**: 429–438.
26. Arikawa-Hirasawa, E, Rossi, SG, Rotundo, RL and Yamada, Y (2002). Absence of acetylcholinesterase at the neuromuscular junctions of perlecan-null mice. *Nat Neurosci* **5**: 119–123.
27. Stum, M, Girard, E, Bangratz, M, Bernard, V, Herbin, M, Vignaud, A *et al.* (2008). Evidence of a dosage effect and a physiological endplate acetylcholinesterase deficiency in the first mouse models mimicking Schwartz-Jampel syndrome neuromyotonia. *Hum Mol Genet* **17**: 3166–3179.
28. Rotundo, RL, Rossi, SG and Anglister, L (1997). Transplantation of quail collagen-tailed acetylcholinesterase molecules onto the frog neuromuscular synapse. *J Cell Biol* **136**: 367–374.
29. Moretti, FA, Chauhan, AK, Iaconcig, A, Porro, F, Baralle, FE and Muro, AF (2007). A major fraction of fibronectin present in the extracellular matrix of tissues is plasma-derived. *J Biol Chem* **282**: 28057–28062.
30. Rooney, JE, Gurpur, PB and Burkin, DJ (2009). Laminin-111 protein therapy prevents muscle disease in the mdx mouse model for Duchenne muscular dystrophy. *Proc Natl Acad Sci USA* **106**: 7991–7996.
31. Hall, ZW and Ralston, E (1989). Nuclear domains in muscle cells. *Cell* **59**: 771–772.
32. Rossi, SG, Vazquez, AE and Rotundo, RL (2000). Local control of acetylcholinesterase gene expression in multinucleated skeletal muscle fibers: individual nuclei respond to signals from the overlying plasma membrane. *J Neurosci* **20**: 919–928.
33. Miner, JH, Go, G, Cunningham, J, Patton, BL and Jarad, G (2006). Transgenic isolation of skeletal muscle and kidney defects in laminin beta2 mutant mice: implications for Pierson syndrome. *Development* **133**: 967–975.
34. Somia, N and Verma, IM (2000). Gene therapy: trials and tribulations. *Nat Rev Genet* **1**: 91–99.
35. Mueller, C and Flotte, TR (2008). Clinical gene therapy using recombinant adeno-associated virus vectors. *Gene Ther* **15**: 858–863.
36. Helbling-Leclerc, A, Zhang, X, Topaloglu, H, Cruaud, C, Tesson, F, Weissenbach, J *et al.* (1995). Mutations in the laminin alpha 2-chain gene (LAMA2) cause merosin-deficient congenital muscular dystrophy. *Nat Genet* **11**: 216–218.
37. Nicole, S, Davoine, CS, Topaloglu, H, Cattolico, L, Barral, D, Beighton, P *et al.* (2000). Perlecan, the major proteoglycan of basement membranes, is altered in patients with Schwartz-Jampel syndrome (chondrodystrophic myotonia). *Nat Genet* **26**: 480–483.
38. Kawahara, G, Okada, M, Morone, N, Ibarra, CA, Nonaka, I, Noguchi, S *et al.* (2007). Reduced cell anchorage may cause sarcolemma-specific collagen VI deficiency in Ullrich disease. *Neurology* **69**: 1043–1049.
39. Okada, T, Nomoto, T, Yoshioka, T, Nonaka-Sarukawa, M, Ito, T, Ogura, T *et al.* (2005). Large-scale production of recombinant viruses by use of a large culture vessel with active gassing. *Hum Gene Ther* **16**: 1212–1218.
40. Okada, T, Shimazaki, K, Nomoto, T, Matsushita, T, Mizukami, H, Urabe, M *et al.* (2002). Adeno-associated viral vector-mediated gene therapy of ischemia-induced neuronal death. *Meth Enzymol* **346**: 378–393.
41. Okada, T, Nonaka-Sarukawa, M, Uchibori, R, Kinoshita, K, Hayashita-Kinoh, H, Nitahara-Kasahara, Y *et al.* (2009). Scalable purification of adeno-associated virus serotype 1 (AAV1) and AAV8 vectors, using dual ion-exchange adsorptive membranes. *Hum Gene Ther* **20**: 1013–1021.
42. Rohr, UP, Wulf, MA, Stahn, S, Steidl, U, Haas, R and Kronenwett, R (2002). Fast and reliable titration of recombinant adeno-associated virus type-2 using quantitative real-time PCR. *J Virol Methods* **106**: 81–88.
43. Engel, AG, Nagel, A, Walls, TJ, Harper, CM and Waisburg, HA (1993). Congenital myasthenic syndromes: I. Deficiency and short open-time of the acetylcholine receptor. *Muscle Nerve* **16**: 1284–1292.
44. Engel, AG and Santa, T (1971). Histometric analysis of the ultrastructure of the neuromuscular junction in myasthenia gravis and in the myasthenic syndrome. *Ann N Y Acad Sci* **183**: 46–63.
45. Engel, AG, Lindstrom, JM, Lambert, EH and Lennon, VA (1977). Ultrastructural localization of the acetylcholine receptor in myasthenia gravis and in its experimental autoimmune model. *Neurology* **27**: 307–315.
46. Otterness, IG and Chang, YH (1976). Comparative study of cyclophosphamide, 6-mercaptopurine, azathiopurine and methotrexate. Relative effects on the humoral and the cellular immune response in the mouse. *Clin Exp Immunol* **26**: 346–354.

SCIENTIFIC REPORTS

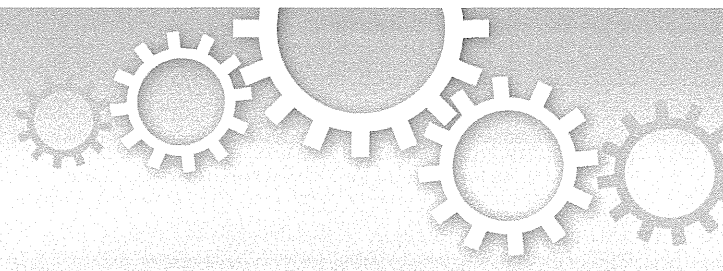

OPEN

SUBJECT AREAS:
MOLECULAR NEUROSCIENCE
NON-CODING RNA'S
GENE REGULATION
MRNA

Received
5 April 2012

Accepted
9 July 2012

Published
24 July 2012

Correspondence and requests for materials should be addressed to G.S. (sobueg@med.nagoya-u.ac.jp) or K.O. (ohnok@med.nagoya-u.ac.jp).

* These authors contributed equally to this work.

Position-dependent FUS-RNA interactions regulate alternative splicing events and transcriptions

Shinsuke Ishigaki[1,4]*, Akio Masuda[2]*, Yusuke Fujioka[1], Yohei Iguchi[1], Masahisa Katsuno[1], Akihide Shibata[2], Fumihiko Urano[3], Gen Sobue[1,4] & Kinji Ohno[2]

[1]Department of Neurology, [2]Division of Neurogenetics, Center for Neurological Diseases and Cancer, Nagoya University Graduate School of Medicine, Nagoya, Japan, [3]Program in Gene Function and Expression, University of Massachusetts Medical School, Worcester, MA, [4]CREST, Japan Science and Technology Agency, Kawaguchi, Japan.

FUS is an RNA-binding protein that regulates transcription, alternative splicing, and mRNA transport. Aberrations of FUS are causally associated with familial and sporadic ALS/FTLD. We analyzed FUS-mediated transcriptions and alternative splicing events in mouse primary cortical neurons using exon arrays. We also characterized FUS-binding RNA sites in the mouse cerebrum with HITS-CLIP. We found that FUS-binding sites tend to form stable secondary structures. Analysis of position-dependence of FUS-binding sites disclosed scattered binding of FUS to and around the alternatively spliced exons including those associated with neurodegeneration such as *Mapt*, *Camk2a*, and *Fmr1*. We also found that FUS is often bound to the antisense RNA strand at the promoter regions. Global analysis of these FUS-tags and the expression profiles disclosed that binding of FUS to the promoter antisense strand downregulates transcriptions of the coding strand. Our analysis revealed that FUS regulates alternative splicing events and transcriptions in a position-dependent manner.

Amyotrophic lateral sclerosis (ALS) is one of the most devastating neurodegenerative disorders characterized by loss of motor neurons in the spinal cord and motor cortex. Approximately 10–20% of ALS patients have a family history. Among them several genes have been identified as a cause or risk-factor for ALS. Interestingly, recently identified ALS-related genes including *TARDBP* encoding the TAR DNA-binding protein (TDP-43) and *FUS* encoding the fused in sarcoma are RNA-binding proteins that regulate RNA metabolisms including gene transcription, RNA splicing, and mRNA transport[1,2]. Mutations in *FUS* have been identified in familial ALS (ALS6). In addition, aberrations of FUS have been linked to the pathogenesis of familial and sporadic ALS as well as frontotemporal lobar degeneration (FTLD)[3,4]. While it remains elusive how aberrations of FUS are linked to the pathogenesis of ALS and FTLD, several lines of evidence suggest that the loss-of-function mechanism is, at least partly, involved in FUS-associated neurodegeneration. First, in autopsied spinal cords and brains of sporadic and familial ALS as well as of FTLD, FUS redistributes into the cytoplasm from the nucleus and accumulates in ubiquitin-positive inclusions[3–5]. Second, artificially introduced mutant FUS proteins in cultured cells are distributed to the cytoplasm from the nucleus[6–9]. This is in contrast to the physiological condition where FUS is localized in the nucleus. Finally, the loss of FUS directly leads to neuronal cell death in drosophila[10] and zebrafish[11].

FUS is a multifunctional protein that is involved in several steps of gene expression regulation especially for transcription and RNA splicing. FUS belongs to the FET family of RNA-binding proteins, which includes FUS, Ewing's sarcoma (EWS), and TATA-binding protein-associated factor (TAFII68)[12]. FUS is present in polymerase II transcription complexes that function in the transcription process[13]. Interestingly, FUS inhibits the acetyltransferase activities of CREB-binding protein (CBP) and p300 on cyclin D1 (*Ccnd1*) in HeLa cells. Both CBP and p300 are co-activators of multiple classes of signal-dependent transcription factors and the TLS/CBP/p300 interactions result in the inhibition of histone-acetyltransferase (HAT) activities followed by repression of transcription[10]. Moreover, FUS is involved in the splicing machinery by cooperating with other splicing factors like serine/arginine-rich (SR) proteins (SC35, SRp75, and TLS-associated SR protein), SRm160, and PTB[14,15]. These observations suggest that compromised effects of FUS on transcription and alternative splicing could lead to neuronal cell degeneration in FUS-associated ALS and FTLD.

In an effort to understand the global roles of FUS on RNA metabolisms in neuronal cells, we analyzed exon arrays of primary cortical neurons after knocking down *Fus*. We also identified FUS-binding RNA segments in the mouse brain using the high-throughput sequencing of RNA isolated by crosslinking immunoprecipitation (HITS-CLIP)[16]. Our analysis revealed the global profiles of FUS-mediated regulations of transcription and pre-mRNA splicing, and the position dependence of FUS-binding sites in regulations of transcription and alternatively splicing.

Results

Silencing of *Fus* in primary cortical neurons. In an effort to identify global profiles of FUS-mediated gene expression and alternative splicing in neurons, we introduced lentivirus expressing shRNA against Fus into primary cortical neurons derived from E15 mouse embryos (Fig. 1a). To exclude possible off-targeting effects, we used two different shRNA, shFus1 and shFus2, and the experiments were performed in triplicate for shFus1 and shFus2 (Fig. 1b). The expression levels of *Fus* were suppressed by more than 80% in both shFus1 and shFus2 by real-time qPCR (Fig. 1c). Immunohistochemistry also showed that the protein levels of FUS were markedly decreased in primary cortical neurons infected with shFus1 and shFus2 (Fig. 1d).

We analyzed gene expression and alternative splicing of *Fus*-silenced primary cortical neurons using the Affymetrix Mouse Exon 1.0 ST Array (GEO accession number, GSE36153). Scatter plots of fold-changes (FC) of gene expressions in cortical neurons showed a correlation coefficient of 0.69 (data not shown). Filtering the gene-level signal intensities with the t-test p-value ≤ 0.1 increased the correlation coefficient to 0.96 (Supplementary Fig. S1a). We further restricted our analysis to 183 genes that had the t-test p-value ≤ 0.05 and FC ≤ 0.67 or $1.5 \leq$ FC for both shFus1 and shFus2. The 21 most altered genes were validated by real-time qPCR and were all indeed differentially expressed in shFus1 and shFus2 (Supplementary Fig. S1c).

We also filtered the exon-level signal intensities with the t-test p-value ≤ 0.1, which gave rise to 3202 exons that were altered by both shFus1 and shFus2 with a correlation coefficient of 0.69 (Supplementary Fig. S1b). We chose 44 exons that were increased by 1.3-fold or more by both shFus1 and shFus2. Similarly, we chose 55 exons that were decreased by 1.5-fold or more by shFus1 and shFus2. We validated 17 exons with increased signals and 20 exons with decreased signals, and all showed altered splicing events by RT-PCR. Especially, we observed altered splicing events in genes associated with neuronal functions and neurodegeneration including *Mapt*, *Camk2a*, and *Fmr1* (Fig. 2 and Supplementary Fig. S2).

We next analyzed Gene Ontology (GO) terms of genes that were regulated by FUS using DAVID 6.7[17,18]. We found that genes for which FUS regulates the expression levels were enriched with GO terms of signaling cascades and metabolic processes. Similarly, genes for which FUS regulates alternative splicing events were enriched with GO terms of vesicle transport, neuronal impulse, and neuronal projection (Table1). FUS is thus likely to exert neuron-specific gene regulations by modulating alternative splicing events rather than gene expressions.

Global identification of FUS-binding RNA segments in mouse brain. We next identified FUS-binding RNA segments *in vivo* by HITS-CLIP (Fig. 1d). As the number of primary cortical neurons that we could obtain from E18 embryos was too small for the HITS-CLIP analysis, we used the mouse cerebrum. In the HITS-CLIP analysis, our first experiment yielded 47,647,724 CLIP tags of 50 nt, of which 17,703,863 were mapped to the mm9 genome using the default parameters with BioScope 1.3.1. A second CLIP experiment yielded 36,282,895 CLIP tags of 50 nt, of which 9,295,669 were mapped to the mouse genome. We only analyzed reads that were aligned uniquely in the genome and removed all potential PCR duplicates using the Avadis NGS software.

Mapping FUS CLIP-tags onto the ENSEMBL annotations revealed that a large fraction of FUS-binding regions were located in introns (Fig. 3a), as previously described[19]. As introns and interegenic regions are longer than the other regions, we normalized distribution of CLIP-tags for the length of each annotation, and found that FUS-binding regions were concentrated in 3′ UTRs as well as introns (Fig. 3b). When CLIP-tags were mapped to the relative positions of each gene, CLIP-tags were enriched close to the 3′ end of a gene and toward the 5′ end of a gene (Fig. 3c). In addition, CLIP-tags were enriched in genes with alternative transcription start/end sites compared to those with constitutive transcription start/end sites.

We next analyzed FUS-binding motifs with the BioProspector software[20], but detected variable motifs that widely varied even by adding, eliminating, or modifying combinations of parameters. Another motif analysis software, MEME[21], also predicted highly variable motifs. Hoell and colleagues reported that FUS binds to stem-and-loop structures with only three loosely conserved nucleotides at the boundaries of a stem and a loop[19]. We thus examined if our CLIP-tagged regions readily form secondary structures. We extracted 30-mer RNA stretches of CLIP-tagged regions and calculated a free energy, δG, of the most stable secondary structure using the mfold program[22]. As expected, the δG's of CLIP-tagged regions were -2.06 ± 3.10 kcal/mol (mean ± SD), whereas those of the controls were -1.50 ± 2.74 kcal/mol ($p < 0.0001$) (Fig. 3d). Stable structures with $\delta G \leq -14.0$ kcal/mol were observed in 28 CLIP-tagged regions and 3 control regions, and the predicted secondary structures are shown in Supplementary Fig. S4. Thus, our CLIP-tagged regions formed stable secondary structures compared to the control regions.

Analysis of position dependence of FUS-binding to splicing targets. FUS-tags were clustered in alternatively spliced splice sites rather than constitutively spliced splice sites, which suggests the essential roles of FUS on regulations of alternative splicing (Fig. 4a). Both exonic and intronic regions were similarly tagged by FUS, but regions around the 3′ and 5′ splice sites were less prominently recognized by FUS, as previously reported[19].

We next analyzed position dependence of FUS-binding to splicing targets and their effects on alternative splicing by comprehensively analyzing the exon array and HITS-CLIP. We analyzed positions of CLIP-tags of 37 FUS-responsive exons that we confirmed by RT-PCR: 17 exons were included and 20 exons were skipped by shRNA (Fig. 2, Supplementary Fig. S2). We combined these exons into a single composite pre-mRNA and made integrated RNA maps from our HITS-CLIP reads mapped to the corresponding genomic regions, as previously described[16,23,24]. The analysis revealed that FUS binding sites were scattered around the alternatively spliced exons (Fig. 4b). Among these, however, it was interesting to note that conspicuous bindings of FUS were observed at ~500 nt upstream of the 3′ end of the downstream intron (arrows in Fig. 4b). The similar peaks were observed when we extended our analysis to 78 FUS-responsive exons detected by the exon array analysis: 54 exons were skipped and 24 exons were included by shRNA (Supplementary Fig. S3). Bindings of FUS to the downstream introns were representatively observed in genes that we validated alternative splicing by RT-PCR (Fig. 2).

***Fus*-binding to the antisense strand at the promoter region downregulates gene expression.** We noticed that CLIP-tags were often located on the antisense strand in each promoter region. A previous report that FUS binds to noncoding RNA (ncRNA) and downregulates transcription of *Ccnd1*[10] prompted us to hypothesize that a transcript arising from the promoter antisense strand is the identity of the ncRNA recognized by FUS. We thus examined if binding of FUS to the promoter antisense strand downregulates

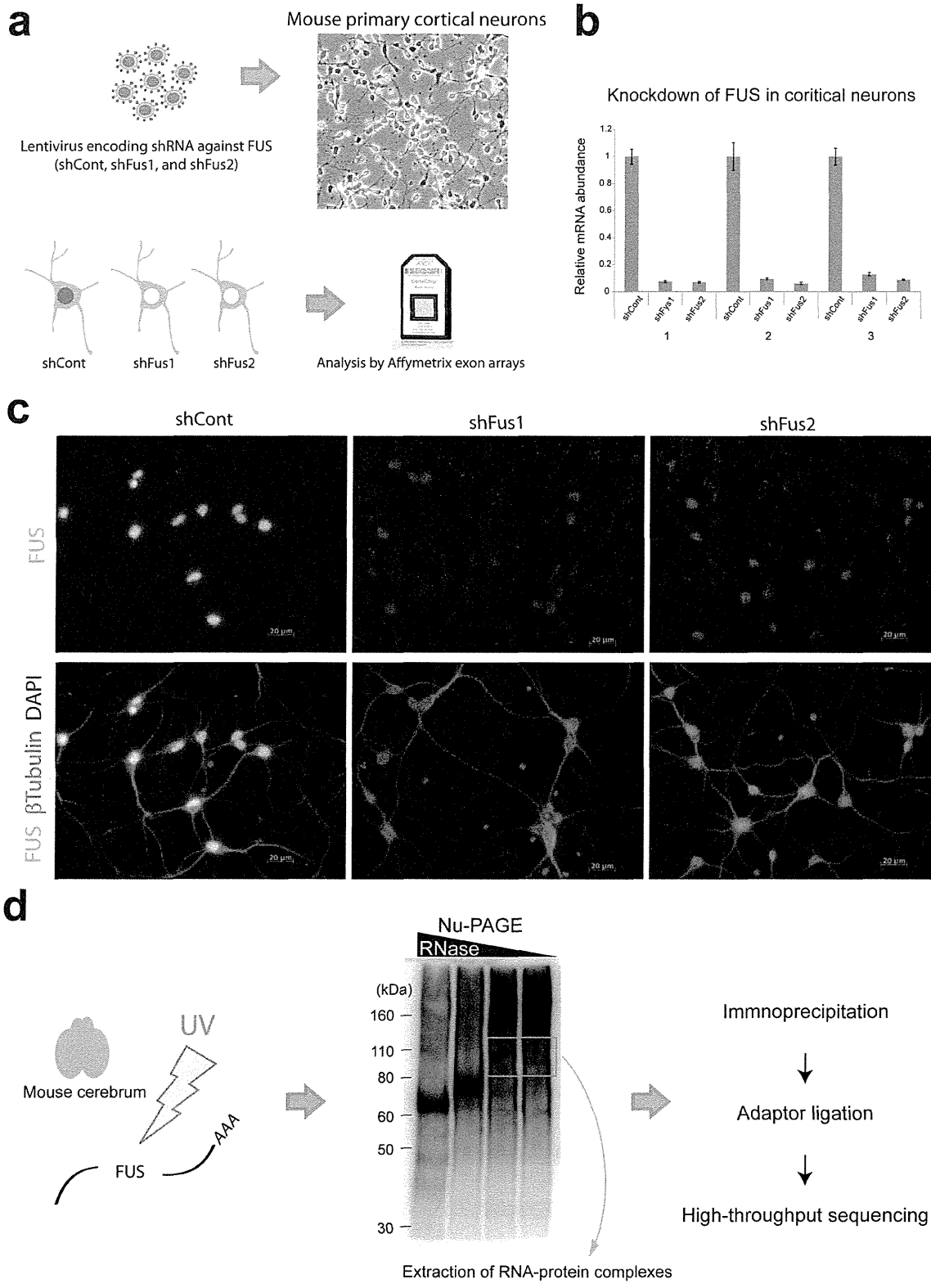

Figure 1 | Experimental schemes. (a) Mouse primary cortical neurons are prepared and infected with lentivirus expressing two different shRNA against FUS (shFus1 and shFus2) and control shRNA (shCont). Total RNA is isolated and analyzed by the Affymetrix Mouse Exon Array. (b) *Fus* is efficiently knocked down in primary cortical neurons, which is evaluated by real-time qRT-PCR. Bars indicate the mean and SD of three experiments. (c) Immunohistchimical analysis using anti-FUS antibody on primary cortical neurons silenced by shFus1, shFus2, and shCont. Cells are fixed and immunostained with anti-FUS antibody, anti-βTubulin antibody, and DAPI. (d) Mouse cerebrum derived from a 12-week-old C57Bl/6 mouse is UV-irradiated at 400 mJ and FUS-bound RNA segments are immuno-precipitated. High-throughput 50 bp single-end sequencing is performed using the SOLiD 3 sequencer.

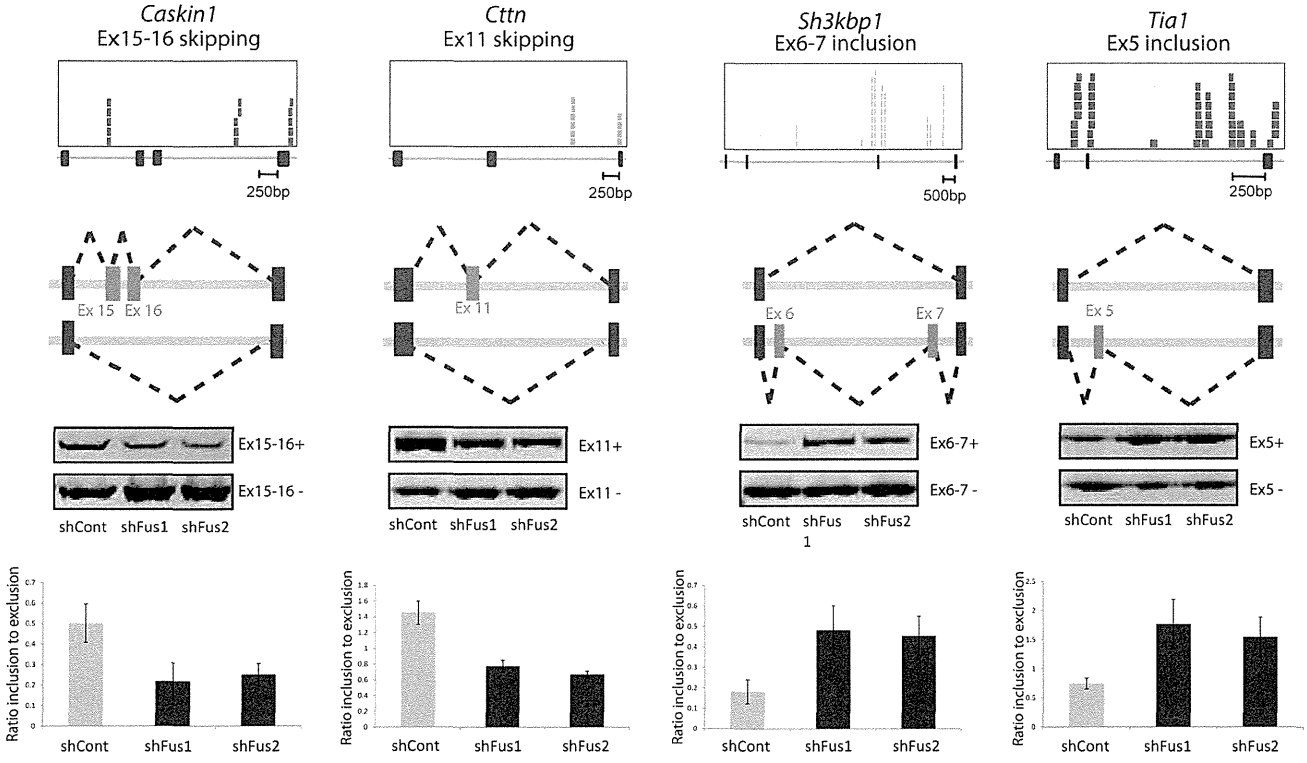

Figure 2 | Four representative FUS-mediated alternative splicing events. The top panels show the positions of CLIP-tags and exon-intron structures. The second panels represent schematic splicing changes mediated by FUS. shCont and shFus lead to the upper and lower splicing events, respectively. The third panels show representative RT-PCR of the indicated exons. The experiments are repeated in quadruplicate using four independent sets of samples. The last panels show densitometric quantification of RT-PCR (n = 4; mean and SD).

gene expression. We analyzed the fold-changes of gene expressions after silencing FUS in primary cortical neurons in the absence or presence of CLIP-tags on the antisense strand upstream of the transcription start sites, and found that the binding of FUS to the promoter antisense strand indeed increases expression of the target genes (Fig. 5a). Eighteen transcriptional start sites of 17 genes carried more than 250 CLIP tags on the promoter antisense strand, and we validated shFus-induced upregulation of transcriptions of four representative genes by realt-ime qPCR (Fig. 5b). The 17 genes, however, did not increase the expression levels more than 1.5-fold after silencing *Fus* according to the exon array analysis, and were not included in our initial validation of the eleven genes in which expression levels were increased with shFus (Supplementary Fig. S1c). On the contrary, the eleven genes scarcely had CLIP-tags on the promoter antisense strand, which suggests the presence of additional and possibly indirect mechanisms that regulate FUS-mediated gene expressions. We also found that genes in which FUS binds to the promoter antisense strand were enriched with GO terms related to reproductive process (Table 1).

Discussion

We globally analyzed FUS-mediated regulations of gene expressions and alternative splicing events using exon arrays. In addition, we globally mapped RNA-FUS interactions *in vivo* by HITS-CLIP and analyzed position dependence of FUS-binding to gene expressions and alternative splicing events.

Collation of the exon-level analysis of exon arrays and CLIP-tags enabled us to draw a normalized complexity map (Fig. 4b). The map disclosed scattered binding of FUS to the upstream and downstream introns with conspicuous binding peaks close to the 3′ end of the downstream intron. A similar peak close to the 3′ end of the downstream intron is observed with PTB and MBNL1 but not with CUGBP1[23,24]. The underlying mechanisms shared by these RNA-binding molecules, however, remain elusive.

Although we could not detect FUS-binding consensus motifs in our CLIP-tags, we found that FUS-binding regions readily form secondary structures. Our observation is consistent with previous reports that FUS binds to stem-and-loop structures[19] and that FUS has a weakly enriched motif endowed with G/C nucleotides, which is present in less than 10% of the FUS-bound sites[25]. *In vitro* SLELX analysis determined that FUS-binding motif is GGUG[26,27]. *Nd1-L*, however, has no GGUG motif but is able to specifically bind to FUS[28]. We assume that FUS binds to specific RNA targets with specific secondary structures, and simple analysis of primary sequences is unlikely to be sufficient.

Divergent transcriptions including bidirectional transcriptions at the promoter regions of protein-coding genes are widely recognized[29,30], although its biological significance is poorly understood. Collation of the gene-level analysis of exon arrays and CLIP-tags on the antisense strands at the promoter regions revealed that binding of FUS to the promoter antisense strand downregulates transcriptions of the coding sense strand (Fig. 5). FUS interacts with CBP and p300 in the presence of ncRNA and inhibits HAT followed by repression of transcription of *Ccnd1*, but the origin of ncRNA was not scrutinized[10]. Our global analysis suggests that binding of FUS to the promoter antisense strand and the subsequent downregulation of transcription of the sense-coding strand is likely to be instrumental in some but not all genes. Recently, Tan and colleagues reported that FUS binds to single-strand DNA at the promoter region, and up- or down-regulates transcriptions[31]. In our CLIP experiments, we needed to degrade DNA using DNase to make a precipitate with anti-FUS antibody. Lack of DNA in our RNA-protein complex was also indicated by that a high concentration of RNase decreased the molecular weight of the RNA-protein complex to that of FUS alone

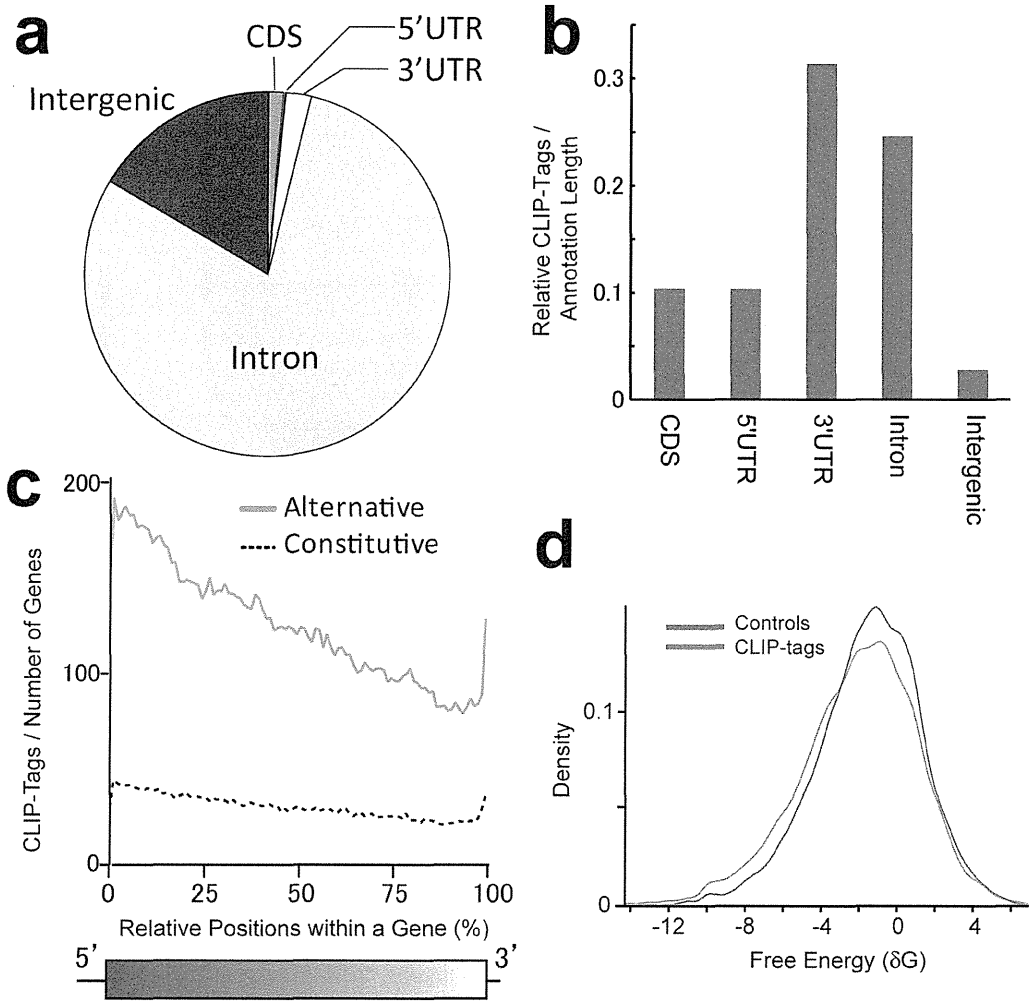

Figure 3 | Annotation mapping of FUS CLIP-tags. (a) Distributions of FUS CLIP-tags. Binding regions are mapped to CDS (coding sequence), 5′ and 3′ UTRs, introns, intergenic regions including tRNA and rRNA genes according to the ENSEMBL version e!61 annotation based on the mouse genome assembly NCBI build 37.1/mm9. Pie-charts show ratios of binding regions mapped to the indicated regions. (b) Distribution of FUS CLIP-tags normalized for the length of each annotation. (c) Distribution of FUS CLIP-tags mapped to the relative positions of each gene. The broken line indicates 12,508 genes with constitutive transcriptional start/end sites, and the solid line indicates 7,477 genes with alternative transcriptional start/end sites. (d) Probability density function of the minimum free energies, δG, of 30-mer stretches of CLIP-tagged regions. CLIP-tagged regions and controls are shown in red and blue lines, respectively.

(Fig. 1d). The underlying mechanisms shared by FUS-binding to single-strand DNA and to the promoter antisense RNA strand need to be further studied.

Involvement of TDP43 and FUS in the pathogenesis of ALS and FTLD suggests that the two diseases are likely to be caused by aberrations of RNA metabolisms[32]. Four additional RNA-binding proteins are causally associated with ALS: senataxin (*SETX*), angiogenin (*ANG*), elongation protein 3 (*ELP3*), and survival motor neuron (*SMN*)[33]. In the present study, we identified that FUS facilitates skipping of *Mapt* exon 10 in primary cortical neurons (Supplementary Fig. S2). *Mapt* encodes Tau protein and inclusion of exon 10 yields 4-repeat Tau (RD4), whereas skipping of exon 10 generates 3-repeat Tau (RD3). It has been reported that the RD4-to-RD3 ratio is increased in neurodegenerative disorders including PSP and FTLD[34,35]. Recently, a large hexanucleotide repeat expansion in intron 1 of *C9ORF72* has been reported in both familial ALS and familial FTLD[36,37]. Abnormally expanded repeats sequestrate MBNL1 in myotonic dystrophy[38], spinocerebellar ataxia type 8[39], and Huntington's disease-like 2[40], and cause RNA gain-of-function pathologies, in which MBNL1 is sequestrated to abnormally expanded repeats, which compromises physiological functions of MBNL1. Thus, aberrations of RNA metabolisms are likely to be a common underlying mechanism shared by familial and sporadic ALS/FLTD. We hope that the global expression profiling and the global CLIP-mapping of FUS in our studies further facilitate discovery of the underlying pathophysiology leading to ALS/FTLD.

Methods

Lentivirus. We designed two different shRNAs against mouse *Fus* as well as a control shRNA. The targeted sequences were 5′-GCAACAAAGCTACGGACAA-3′ for shRNA/FUS1 (shFus1); 5′-GAGTGGAGGTTATGGTCAA-3′ for shRNA/FUS2 (shFus2); and 5′-AATTCTCCGAACGTGTCACGT-3′ for shRNA/control (shCont). These were cloned into a lentiviral shRNA vector (pLenti-RNAi-X2 puro DEST, w16-1, a kind gift from Dr. Eric Campeau at Resverlogix Corp.). Lentivirus was prepared following the Campeu's protocols[41]. Briefly, lentiviral particles were produced in HEK293T cells by transfection using Lipofectamine 2000 (Invitrogen). Lentivirus-containing supernatant was collected at 48 hours after transfection, and stored at -80°C. A titer of lentivirus was measured using NucleoSpin RNA Virus kit (Clontech Laboratories).

Primary cortical neurons. Mouse studies were approved by the Animal Care and Use Committee of the Nagoya University Graduate School of Medicine. Mouse fetal brain

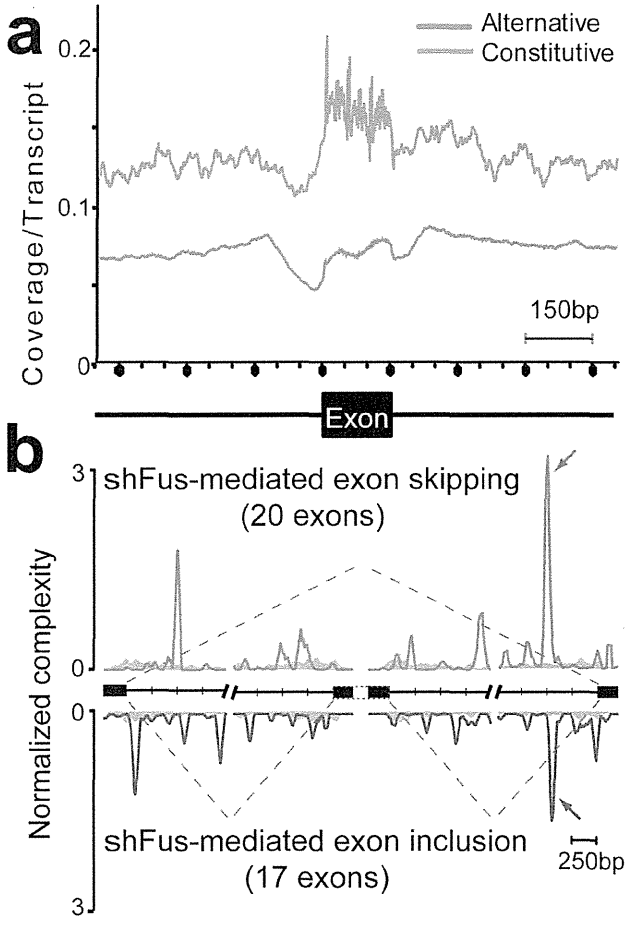

Figure 4 | Mapping of CLIP-tags on exon-intron structures. (a) Distribution of CLIP-tags on constitutively or alternatively spliced exons and the flanking intronic regions. The abscissa indicates an intron-exon-intron structure. The sizes of all the exons are normalized to 150 nucleotides. The number of exonic CLIP-tags is also normalized accordingly. Intronic CLIP-tags within 1,000 nucleotides upstream or downstream of exons are indicated. The number of CLIP-tags is normalized for the number of transcripts belonging to each category of constitutive and alternative exons. (b) Normalized complexity map of FUS-dependent splice sites. shFus-mediated alternative splicing events are compiled. Arrows point to conspicuous peaks at ~500 nt upstream of the 3′ end of the downstream intron. Shaded areas indicate an average of 100 sets of normalized complexity of 20 randomly selected constitutive exons.

was taken from C57BL/6 mouse embryos at E15. After removing meninges cortical tissue was dissociated into a single-cell suspension by Sumilon dissociation solution (Sumitomo Bakelite, Tokyo Japan). Cells were plated at a density of 1.5 x 10^6 cells in a 60 mm-well culture plate with the medium containing 0.5x Sumilon nerve-culture medium (Sumitomo Bakelite), 0.5x Neurobasal medium, 1% FBS, 0.5x B27 supplements (Invitrogen), 0.5x Glutamax, 5 μg/ml of BDNF, 5 μg/ml of CNTF, and 0.5% Pen-Strep. A day after plating (day 2), neurons were supplemented with 10 ng/μl of AraC and incubated overnight. On day 5, neurons were infected with 2x10^{10} copies/well (1.5x10^7 copies/μl) of lentivirus expressing shRNA against mouse *Fus* (shFus1 or shFus2) or control (shCont). After 4 hr of infection, the virus media was removed. Neurons were then cultured for 6 additional days, and were harvested on day 11 followed by RNA extraction and cDNA synthesis. Each knock-down experiment was performed in triplicate for each microarray analysis. For immunohistochemistry we used anti-FUS antibody (A300-293A, Bethyl Laboratories), anti-βTubulin antibody (TU20, Santa Cruz), and DAPI.

Microarray analysis. Total RNA was extracted from primary cortical neurons by the RNeasy Mini kit (Qiagen). We confirmed that the RNA integrity numbers (RIN) were all above 7.0. We synthesized and labeled cDNA fragments from 100 ng of total RNA using the GeneChip WT cDNA Synthesis Kit (Ambion). Hybridization and signal acquisition of the GeneChip Mouse Exon 1.0 ST exon array (Affymetrix) were

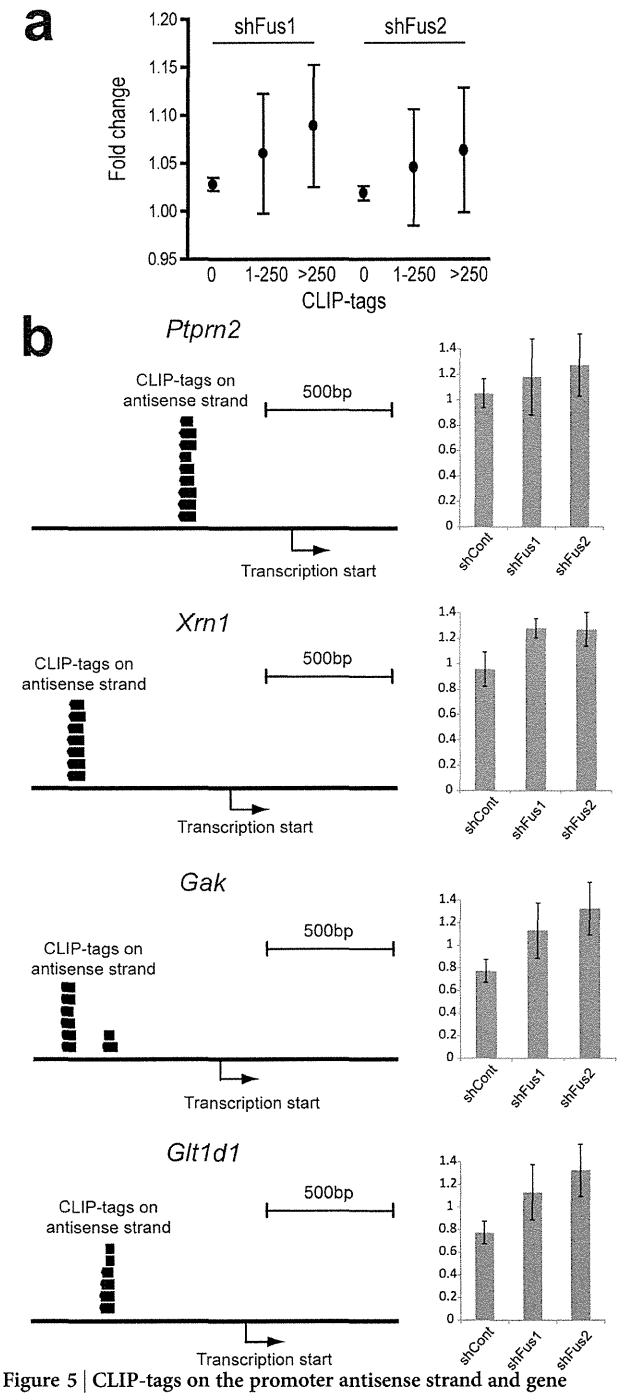

Figure 5 | CLIP-tags on the promoter antisense strand and gene expression profiles. (a) The numbers of CLIP-tags on the antisense strand at 1 to 700 nucleotides upstream of the transcription start sites of each gene are divided into three categories according to the partitioning functionality of the JMP 8.0 software. Fold-changes of gene expression levels with shFus1 and shFus2 are calculated for each category. Means and SEs are plotted. The numbers of transcription start sites are 2390 for no tag, 53 for 1-250 tags, and 18 for more than 250 tags. The number of CLIP-tags represents the total number of nucleotides covered by the tags. No statistical difference is observed for each dataset with the one-way ANOVA analysis. (b) Four representative genes, *Ptprn2*, *Xrn1*, *Gak*, and *Glt1d1*, for which more than 250 CLIP-tags are bound to the promoter antisense strand, are validated by real-time qPCR. Changes in gene expression levels in cortical neurons after knocking down *Fus* with shFus1 and shFus2 are indicated by means and SDs (n = 3).

Table 1 | Gene Ontology terms enriched in FUS-associated genes

GO ID	GO_TERM_BP_FAT	P-value
Gene expression		
GO:0007242	Intracellular signaling cascade	0.0083
GO:0006796	Phosphate metabolic process	0.0115
GO:0006793	Phosphorus metabolic process	0.0115
GO:0007265	Ras protein signal transduction	0.0163
GO:0046486	Glycerolipid metabolic process	0.0296
Alternative splicing		
GO:0016192	Vesicle-mediated transport*	0.0077
GO:0006887	Exocytosis	0.0081
GO:0019226	Transmission of nerve impulse*	0.0101
GO:0016044	Membrane organization	0.0188
GO:0048812	Neuron projection morphogenesis*	0.0283
Promoter antisense strand		
GO:0032504	Multicellular organism reproduction	0.0060
GO:0048609	Reproductive process	0.0060
GO:0006350	Transcription	0.0092
GO:0007276	Gamete generation	0.0145
GO:0043933	Macromolecular complex organization	0.0205

GO terms with the five best P-values in each category are indicated.
*GO terms with neuron-specific functionalities.

performed according to the manufacturer's instructions. Each array experiment was performed in triplicate. The exon-level and gene-level signal intensities were normalized by the RMA and iterPLIER methods, respectively, using the Expression Console 1.1.2 (Affymetrix). We followed the gene annotation of the ENSEMBL version e!61, which was based on the mouse genome assembly NCBI build 37.1/mm9. All microarray data were registered in the Gene Expression Omnibus with an accession number of GSE36153.

We compared the gene-level signal intensities of three controls treated with shCont and three samples treated either with shFus1 or shFus2 using the Student's t-test. Among the 21,603 genes on the mouse exon array, 1,814 genes had the t-test p-values ≤ 0.10 for both shFus1 and shFus2, and the correlation coefficient of the fold-changes became 0.963 between shFu1 and shFus2 (Supplementary Fig. S1a). By applying the t-test p-values ≤ 0.01 for both shFus1 and shFus2, we obtained 1,500 genes, the expression levels of which were altered by knocking down *Fus*. We also analyzed alternative splicing profiles by filtering the exon-level signal intensities with the t-test p-value ≤ 0.1, which gave rise to 3,202 exons that were altered by both shFus1 and shFus2 with the correlation coefficient of 0.925 (Supplementary Fig. S1b).

RT-PCR for alternative splicing analysis. Total RNA was isolated from cells using RNeasy Mini Kit (Qiagen) followed by DNaseI (Qiagen) treatment. cDNA was synthesized from 1 μg of total RNA with the Oligo-dT primer (Promega). Primers for each candidate exon were designed using Primer3 software (http://frodo.wi.mit.edu/primer3/input.htm). The sequences of primers were shown in Table S1. Semi-quantitative RT-PCR was performed using Ex Taq (Takara) at 25-30 cycles at 98°C for 10 sec, 60°C for 30 sec, and 72°C for 1 min. PCR products was electrophoresed on a 15% acrylamide gel and stained with ethidium bromide. The intensity of each band was measured by Multi Gage software (Fujifilm).

Real-time qPCR for gene expression analysis. Total RNA was isolated from cells using RNeasy Mini Kit (Qiagen) and reverse transcribed using 1 μg of total RNA with Oligo-dT primer. For the thermal cycle reaction, the CFX96 system (BioRad) was used at 95°C for 3 min, then 40 cycles at 95°C for 10 sec and 55°C for 30 sec.

The relative amount for each transcript was calculated by drawing a standard curve of cycle thresholds for serial dilutions of cDNA samples and normalized to the amount of β-actin. The PCR was performed in triplicate for each sample, after which all experiments were repeated twice. The sets of primers (Table S1) and iQ SYBR Green Supermix (BioRad) were used for real-time qPCR.

HITS-CLIP analysis. Mouse cerebrum derived from 12-week-old C57BL/6 mice was UV-irradiated at 400 mJ and CLIP was performed as previously described[24]. High-throughput 50-bp single-end sequencing was performed with the SOLiD 3 sequencer (Life Technologies) using one quad of a SOLiD sequencing slide for each sample. All HITS-CLIP data were registered in NCBI SRA. Sequences of RNA oligonucleotide adaptors and PCR primers used for HITS-CLIP analysis were as follows:

5′-RNA linker 5′-CCACUACGCCUCCGCUUUCCUCUCUAUGGGCAGUCG-GUGAU-3′

3′-RNA linker phospho-5′-AGAGAAUGAGGAACCCGGGGCAGUU-3′-amino

RT Primer 5′- CCCGGGTTCCTCATTCTCTCGCCTTGGCCGTACAG-3′

Forward PCR Primer 5′- CCACTACGCCTCCGCTTTCCTCTCTATG-3′

Reverse PCR Primer 5′-CTGCCCCGGGTTCCTCATTCT-3′

Bioinformatics analysis. SOLiD reads were mapped to the mouse genome (NCBI build 37.1/mm9) with default parameters using the BioScope 1.3.1 (Life Technologies). We next removed multiply aligned reads, unreliable reads, and PCR duplicates with Avadis NGS software 1.3 (Strand). We analyzed the uniquely aligned reads according to the ENSEMBL version e!61 gene annotations of the mouse genome (NCBI build 37.1/mm9) by writing and running Perl and Excel VBA programs, as well as by running BEDTools utilities[42].

We extracted CLIP-tagged regions using the enrichment functionality of Avadis NGS. Motifs of the tagged regions were analyzed by BioProspector[20] and MEME[21]. As these motif analysis tools gave rise to highly variable motifs, we extracted 17,385 30-mer RNA stretches of the CLIP-tagged regions by moving a 30-mer window every five nucleotides, and calculated the free energy, δG, of the most stable secondary structure using the mfold program[22]. We similarly calculated the free energies of control sequences for which nucleotide sequences were scrambled from the 30-mer stretches of the CLIP-tagged regions.

We identified 2,461 distinct transcription start sites in the 1,500 genes, the transcription levels of which were significantly altered by both shFus1 and shFus2. We counted CLIP tags on the antisense strand at 1 to 700 nucleotides upstream of each transcription start site. We analyzed the expression profiles of primary cortical neurons after knocking down *Fus* in relation to the number of CLIP tags on the antisense strand at the promoter region.

Normalized complexity maps of FUS-RNA interactions were generated as previously described[24]. For the control, normalized complexity map was similarly generated by analyzing 100 sets of 20 constitutive exons that were randomly selected from 118,969 constitutive exons in the mouse genome. To identify enriched Gene Ontology terms, we used the Database for Annotation, Visualization and Integrated Discovery (DAVID 6.7)[17,18].

1. Strong, M. J. & Volkening, K. TDP-43 and FUS/TLS: sending a complex message about messenger RNA in amyotrophic lateral sclerosis? *FEBS J* 278, 3569–3577 (2011).
2. Lagier-Tourenne, C. & Cleveland, D. W. Rethinking ALS: the FUS about TDP-43. *Cell* 136, 1001–1004 (2009).
3. Kwiatkowski, T. J., Jr. *et al.* Mutations in the FUS/TLS gene on chromosome 16 cause familial amyotrophic lateral sclerosis. *Science* 323, 1205–1208 (2009).
4. Vance, C. *et al.* Mutations in FUS, an RNA processing protein, cause familial amyotrophic lateral sclerosis type 6. *Science* 323, 1208–1211 (2009).
5. Deng, H. X. *et al.* FUS-immunoreactive inclusions are a common feature in sporadic and non-SOD1 familial amyotrophic lateral sclerosis. *Ann Neurol* 67, 739–748 (2010).
6. Bosco, D. A. *et al.* Mutant FUS proteins that cause amyotrophic lateral sclerosis incorporate into stress granules. *Hum Mol Genet* 19, 4160–4175 (2010).
7. Dormann, D. *et al.* ALS-associated fused in sarcoma (FUS) mutations disrupt Transportin-mediated nuclear import. *EMBO J* 29, 2841–2857 (2010).
8. Ito, D., Seki, M., Tsunoda, Y., Uchiyama, H. & Suzuki, N. Nuclear transport impairment of amyotrophic lateral sclerosis-linked mutations in FUS/TLS. *Ann Neurol* 69, 152–162 (2011).
9. Kino, Y. *et al.* Intracellular localization and splicing regulation of FUS/TLS are variably affected by amyotrophic lateral sclerosis-linked mutations. *Nucleic Acids Res* 39, 2781–2798 (2011).
10. Wang, X. *et al.* Induced ncRNAs allosterically modify RNA-binding proteins in cis to inhibit transcription. *Nature* 454, 126–130 (2008).
11. Kabashi, E. *et al.* FUS and TARDBP but not SOD1 interact in genetic models of amyotrophic lateral sclerosis. *PLoS Genet* 7, e1002214 (2011).
12. Guipaud, O. *et al.* An in vitro enzymatic assay coupled to proteomics analysis reveals a new DNA processing activity for Ewing sarcoma and TAF(II)68 proteins. *Proteomics* 6, 5962–5972 (2006).
13. Bertolotti, A., Lutz, Y., Heard, D. J., Chambon, P. & Tora, L. hTAF(II)68, a novel RNA/ssDNA-binding protein with homology to the pro-oncoproteins TLS/FUS and EWS is associated with both TFIID and RNA polymerase II. *EMBO J* 15, 5022–5031 (1996).
14. Meissner, M., Lopato, S., Gotzmann, J., Sauermann, G. & Barta, A. Proto-oncoprotein TLS/FUS is associated to the nuclear matrix and complexed with splicing factors PTB, SRm160, and SR proteins. *Exp Cell Res* 283, 184–195 (2003).
15. Yang, L., Embree, L. J., Tsai, S. & Hickstein, D. D. Oncoprotein TLS interacts with serine-arginine proteins involved in RNA splicing. *J Biol Chem* 273, 27761–27764 (1998).
16. Licatalosi, D. D. *et al.* HITS-CLIP yields genome-wide insights into brain alternative RNA processing. *Nature* 456, 464–469 (2008).
17. Huang da, W., Sherman, B. T. & Lempicki, R. A. Systematic and integrative analysis of large gene lists using DAVID bioinformatics resources. *Nat Protoc* 4, 44–57 (2009).
18. Dennis, G., Jr. *et al.* DAVID: Database for Annotation, Visualization, and Integrated Discovery. *Genome Biol* 4, P3 (2003).
19. Hoell, J. I. *et al.* RNA targets of wild-type and mutant FET family proteins. *Nat Struct Mol Biol* 18, 1428–1431 (2011).
20. Liu, X., Brutlag, D. L. & Liu, J. S. BioProspector: discovering conserved DNA motifs in upstream regulatory regions of co-expressed genes. *Pac Symp Biocomput* 127–138 (2001).
21. Bailey, T. L. & Elkan, C. The value of prior knowledge in discovering motifs with MEME. *Proc Int Conf Intell Syst Mol Biol* 3, 21–29 (1995).

22. Zuker, M. Mfold web server for nucleic acid folding and hybridization prediction. *Nucleic Acids Res* 31, 3406–3415 (2003).
23. Xue, Y. *et al.* Genome-wide analysis of PTB-RNA interactions reveals a strategy used by the general splicing repressor to modulate exon inclusion or skipping. *Mol Cell* 36, 996–1006 (2009).
24. Masuda, A. *et al.* CUGBP1 and MBNL1 preferentially bind to 3′ UTRs and facilitate mRNA decay. *Sci Rep* 2, 209 (2012).
25. Colombrita, C. *et al.* TDP-43 and FUS RNA-binding proteins bind distinct sets of cytoplasmic messenger RNAs and differently regulate their post-transcriptional fate in motoneuron-like cells. *J Biol Chem* Epub (2012).
26. Lerga, A. *et al.* Identification of an RNA binding specificity for the potential splicing factor TLS. *J Biol Chem* 276, 6807–6816 (2001).
27. Iko, Y. *et al.* Domain architectures and characterization of an RNA-binding protein, TLS. *J Biol Chem* 279, 44834–44840 (2004).
28. Fujii, R. & Takumi, T. TLS facilitates transport of mRNA encoding an actin-stabilizing protein to dendritic spines. *J Cell Sci* 118, 5755–5765 (2005).
29. Core, L. J., Waterfall, J. J. & Lis, J. T. Nascent RNA sequencing reveals widespread pausing and divergent initiation at human promoters. *Science* 322, 1845–1848 (2008).
30. Seila, A. C. *et al.* Divergent transcription from active promoters. *Science* 322, 1849–1851 (2008).
31. Tan, A. Y., Riley, T. R., Coady, T., Bussemaker, H. J. & Manley, J. L. TLS/FUS (translocated in liposarcoma/fused in sarcoma) regulates target gene transcription via single-stranded DNA response elements. *Proc Natl Acad Sci U S A* Epub (2012).
32. Lagier-Tourenne, C., Polymenidou, M. & Cleveland, D. W. TDP-43 and FUS/TLS: emerging roles in RNA processing and neurodegeneration. *Hum Mol Genet* 19, R46–64 (2010).
33. van Blitterswijk, M. & Landers, J. E. RNA processing pathways in amyotrophic lateral sclerosis. *Neurogenetics* 11, 275–290 (2010).
34. Hong, M. *et al.* Mutation-specific functional impairments in distinct tau isoforms of hereditary FTDP-17. *Science* 282, 1914–1917 (1998).
35. Yoshida, M. Cellular tau pathology and immunohistochemical study of tau isoforms in sporadic tauopathies. *Neuropathology* 26, 457–470 (2006).
36. Renton, A. E. *et al.* A hexanucleotide repeat expansion in C9ORF72 is the cause of chromosome 9p21-linked ALS-FTD. *Neuron* 72, 257–268 (2011).
37. DeJesus-Hernandez, M. *et al.* Expanded GGGGCC hexanucleotide repeat in noncoding region of C9ORF72 causes chromosome 9p-linked FTD and ALS. *Neuron* 72, 245–256 (2011).
38. Ranum, L. P. & Cooper, T. A. RNA-mediated neuromuscular disorders. *Annu Rev Neurosci* 29, 259–277 (2006).
39. Moseley, M. L. *et al.* Bidirectional expression of CUG and CAG expansion transcripts and intranuclear polyglutamine inclusions in spinocerebellar ataxia type 8. *Nat Genet* 38, 758–769 (2006).
40. Rudnicki, D. D. *et al.* Huntington's disease--like 2 is associated with CUG repeat-containing RNA foci. *Ann Neurol* 61, 272–282 (2007).
41. Campeau, E. *et al.* A versatile viral system for expression and depletion of proteins in mammalian cells. *PLoS One* 4, e6529 (2009).
42. Quinlan, A. R. & Hall, I. M. BEDTools: a flexible suite of utilities for comparing genomic features. *Bioinformatics* 26, 841–842 (2010).

Acknowledgements

This work was supported by Grants-in-Aid from the MEXT/JST, MEXT/ICBIT, CREST/JST, SRPBS/JST, and MHLW of Japan. We are grateful to Dr. Kunio Ihara at the Center for Gene Research of Nagoya University for the SOLiD sequencing analysis.

Author contributions

S.I., A.M., Y.F., Y.I., and M.K. performed the experiments. S.I., A.M., A.S., and K.O. analyzed the data. S.I., A.M., F.U., G.S. and K.O. prepared the manuscript. All authors reviewed the manuscript.

Additional information

Accession code: The HITS-CLIP and microarray data were registered in the NCBI Gene Expression Omnibus database with accession numbers GSE37190 and GSE36153, respectively.

Supplementary information accompanies this paper at http://www.nature.com/scientificreports

Competing financial interests: The authors declare no competing financial interests.

How to cite this article: Ishigaki, S. *et al.* Position-dependent FUS-RNA interactions regulate alternative splicing events and transcriptions. *Sci. Rep.* 2, 529; DOI:10.1038/srep00529 (2012).

RESIDENT & FELLOW SECTION

Section Editor
Mitchell S.V. Elkind, MD, MS

Teaching NeuroImages: Unilateral arm and contralateral leg amyotrophy in FSHD

Unusual presentation

Kazuma Sugie, MD, PhD
Yukiko K. Hayashi, MD, PhD
Kanako Goto, BS
Ichizo Nishino, MD, PhD
Satoshi Ueno, MD, PhD

Correspondence & reprint requests to Dr. Sugie: ksugie@naramed-u.ac.jp

Figure **Photographs and muscle imaging findings of the whole body in a patient with facioscapulohumeral muscular dystrophy (FSHD)**

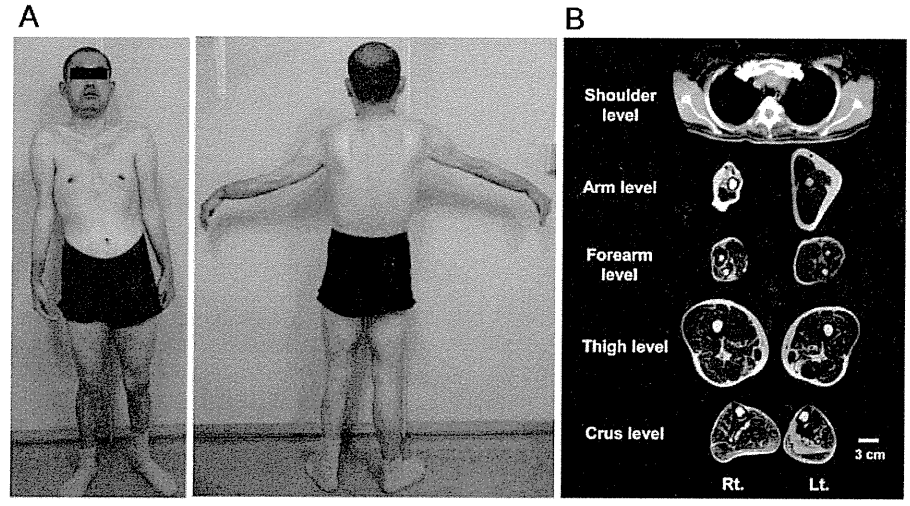

(A) The patient predominantly shows remarkable atrophy of the right facial, shoulder girdle, and arm muscles and of the left leg muscles. He put his weight on his right leg (with permission). (B) CT of the shoulder and T2-weighted MRI of the 4 limbs. CT shows atrophy of the right shoulder girdle and greater pectoral muscles. Amyotrophy and replacement of muscle tissue by fat is asymmetrically pronounced in the right sides of the biceps and triceps brachii and forearm, and the left sides of the femoral and calf muscles on MRI.

A 43-year-old, right-handed man noticed right arm weakness at age 23, followed by the development of left leg weakness and claudication. Although his deceased mother was considered to have had facioscapulohumeral muscular dystrophy (FSHD), her clinical symptoms were unclear. Neurologic examinations and imaging showed predominant weakness/atrophy in the right arm and left leg (figure). EMG demonstrated predominant myopathic changes in the right arm and left leg. No involvement of the CNS or peripheral nerves was apparent. Southern blotting analysis for FSHD revealed a 20-kb *Eco*RI fragment on 4q35 (normal >35 kb).

Asymmetric muscle involvement is a characteristic feature of FSHD.[1,2] Asymmetry might depend not only on handedness, but also on genetic predisposition.

REFERENCES

1. Olsen DB, Gideon P, Jeppesen TD, Vissing J. Leg muscle involvement in facioscapulohumeral muscular dystrophy assessed by MRI. J Neurol 2006;253:1437–1441.
2. Brouwer OF, Padberg GW, van der Ploeg RJ, Ruys CJ, Brand R. The influence of handedness on the distribution of muscular weakness of the arm in facioscapulohumeral muscular dystrophy. Brain 1992;115:1587–1598.

From the Department of Neurology (K.S., S.U.), Nara Medical University School of Medicine, Nara; and Department of Neuromuscular Research (K.S., Y.K.H., K.G., I.N.), National Institute of Neuroscience, National Center of Neurology and Psychiatry (NCNP), Kodaira, Tokyo, Japan.
The authors report no disclosures relevant to the manuscript. Go to Neurology.org for full disclosures.

INTERNAL MEDICINE

□ CASE REPORT □

Characterization of Dermatomyositis with Coexistence of Anti-Jo-1 and Anti-SRP Antibodies

Kazuma Sugie, Yasuyo Tonomura and Satoshi Ueno

Abstract

We describe a patient with dermatomyositis who presented with rapidly developing severe muscle weakness complicated by massive pleural effusion with interstitial lung disease. Myopathological analysis was suggestive of dermatomyositis. This patient showed both anti-Jo-1 and anti-SRP antibodies in serum. To our knowledge, the coexistence of these two myositis-specific autoantibodies (MSA) is considered extremely rare and is clearly an exception to the rule of having only one MSA. Our findings provide compelling evidence that the coexistence of these two MSAs may lead to more severe clinical symptoms, interacting in a complex fashion, thus expanding the clinical spectrum of idiopathic inflammatory myopathy.

Key words: idiopathic inflammatory myopathy, dermatomyositis, pleural effusion, myositis-specific autoantibody, anti-Jo-1 antibody, anti-SRP antibody

(Intern Med 51: 799-802, 2012)
(DOI: 10.2169/internalmedicine.51.6566)

Introduction

Idiopathic inflammatory myopathies such as polymyositis (PM) and dermatomyositis (DM) are systemic autoimmune connective tissue diseases characterized by chronic muscle inflammation with involvement of various organs (1). The pathogenesis of PM/DM is unknown, but autoantibodies directed against various cellular constituents have been identified in patients with PM/DM. Some autoantibodies found almost exclusively in PM/DM are known as myositis-specific autoantibodies (MSA), including anti-Jo-1 (histidyl tRNA synthetase) antibody, anti-PL-7 antibody, anti-signal recognition particle (SRP) antibody, anti-Mi-2 antibody, and anti-CADM-140 antibody. Each MSA is associated with a set of unique clinical features (2, 3).

We describe a 61-year-old man with DM who presented with severe muscle involvement characterized by rapidly developing proximal weakness, culminating in severe disability. He also showed massive pleural effusion with interstitial lung disease (ILD). Interestingly, both anti-Jo-1 and anti-SRP antibodies were positive in his serum. To our knowledge, the coexistence of these two types of MSA is considered extremely rare. Only one other case of idiopathic inflammatory myopathy with these two MSAs has been described in a recent report (4). Our findings suggest that coexistence of these two MSAs is associated with specific clinicopathological features.

Case Report

A 61-year-old man was admitted in June because of a 1-month history of rapidly progressive severe weakness of all four extremities. His skin was discolored, and he had dyspnea. The past history was noncontributory to the present illness. On admission, he presented with difficulty in getting up from bed and lifting his arms above his head. Physiological examination showed severe symmetric proximal weakness (less than grade 3 according to the Medical Research Council scale) of all four extremities. There were no other motor deficits. Sensory and stretch reflexes were normal. Erythematous rashes were present on the arms, trunk, legs, and face, including a typical heliotrope rash and Gottron's papules.

Laboratory examinations showed very high levels of creatine kinase (CK) (5,685 IU/L; normal: <160) in serum. The erythrocyte sedimentation rate and C-reactive protein were slightly elevated (80 mm/hr, <10; 2.6 IU/L, <0.1). Serum

Department of Neurology, Nara Medical University School of Medicine, Japan
Received for publication September 15, 2011; Accepted for publication December 5, 2011
Correspondence to Dr. Kazuma Sugie, ksugie@naramed-u.ac.jp

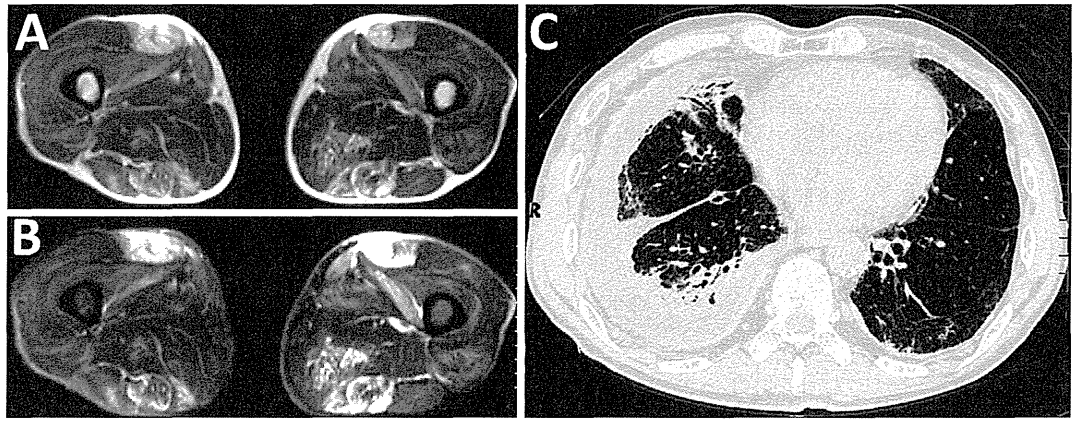

Figure 1. **Magnetic resonance images of the thighs (A, B) and computed tomographic scans of the chest (C). T2-weighted (A) and T2-short-tau inversion recovery (STIR) images (B) showed diffuse high intensity in the frontal and dorsal aspects of both thigh muscles, suggesting intramuscular inflammation and edema. Chest images showed massive pleural effusion with interstitial lung disease (C).**

antinuclear antibody was detected, accompanied by positivity for both anti-Jo-1 and anti-SRP antibodies, but negativity for other MSA, such as anti-PL-7 antibody. Among myositis-associated autoantibodies, anti-SS-A, anti-SS-B, anti-U1-RNP, and anti-Scl-70 antibodies were not detected. Electromyography showed short duration, small amplitude, polyphagic motor unit potentials with fibrillation potentials in the upper and lower limb muscles. Magnetic resonance images of the skeletal muscle showed diffuse inflammation and edema, most prominent in the proximal muscles of all four extremities (Fig. 1A, 1B). Computed tomography of the lung showed severe changes characteristic of ILD, with massive pleural effusion (Fig. 1C). The pleural fluid revealed exudate with no evidence of malignancy. A biopsy of the femoral muscle showed many necrotic and regenerative fibers with marked perimysial cell infiltration (Fig. 2). The infiltrating CD4+/CD8+ T cell ratio at perimysial sites (mean ± SD) was 1.58±0.28. Characteristic perifascicular muscle fiber atrophy was seen. Strong major histocompatibility complex class I (MHC-I) expression, especially in perifascicular atrophic fibers, was positive in cytoplasm. There was no expression of CD8/MHC-I complex, which suggested that CD8+ T cells invaded non-necrotic fibers that express MHC-I antigen. Expression of membrane attack complex (MAC) was present on endomysial capillaries, but not on necrotic fibers. These pathological findings of muscle suggested DM rather than PM.

The patient was given a diagnosis of DM with ILD. He initially received oral prednisone (1 mg/kg/day) for a month, with tapering to 20 mg/day over the course of the next three months. His muscle strength gradually improved, but he was still unable to move independently. Respiratory difficulties and pleural effusion were mildly decreased. The erythematous rashes decreased, but persisted slightly. Four months after the start of treatment, a progressive gastric cancer (papillary adenocarcinoma, stage IIIA) was diagnosed. A gastrectomy was thus performed. Subsequently, the muscle weakness and respiratory difficulties worsened despite an increase in the dose of steroids. One year after gastrectomy, the patient died of progressive ILD with massive pleural effusion and multiple liver metastases from gastric cancer.

Discussion

We described a patient with idiopathic inflammatory myopathy accompanied by ILD with massive pleural effusion, who presented with rapidly developing severe proximal weakness and respiratory difficulty. His skin lesions were suggestive of DM. Histopathological examination of a muscle specimen revealed many necrotic and regenerative fibers with marked perimysial cell infiltration, predominantly involving CD4+ T cells. Strong MHC-I expression by perifascicular atrophic fibers was consistent with DM (5). In addition, expression of MAC on endomysial capillaries, but not on necrotic fibers in our patient distinguished DM from paraneoplastic necrotizing myopathy (6). Collectively, these histopathological findings of muscle, including no expression of CD8/MHC-I complex, suggested DM rather than PM.

Interestingly, the present patient showed both anti-Jo-1 and anti-SRP antibody in his serum. The presence of these two MSAs is considered extremely rare and is clearly an exception to the rule of having only one MSA in association with PM/DM (7). To our knowledge, the coexistence of these MSAs has only been documented one time previously (4). That patient had severe muscle weakness and ILD, characterized by the presence of both anti-Jo-1 and anti-SRP antibody. Although the reason for this association and the pathogenic roles of these two MSAs are unclear, MSA may play a key, yet indirect part in the etiology of PM/DM.

Each MSA is associated with a set of unique clinical features (2, 3). Anti-Jo-1 antibody, one of the aminoacyl tRNA synthetases antibodies, is closely related to PM/DM, which

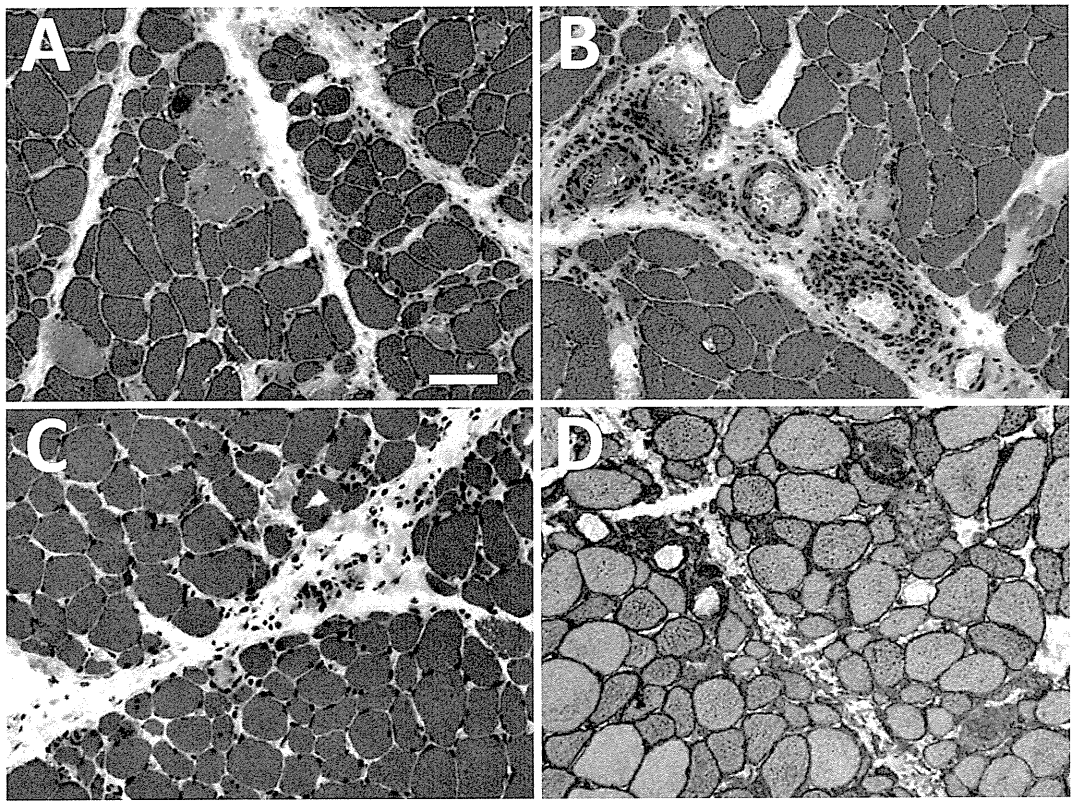

Figure 2. **Light microscopic findings of femoral muscle specimens (A-D). A biopsy of the femoral muscle showed many necrotic and regenerative fibers (A). Marked perivascular lymphocytic inflammations were found in perimysial tissue (B). Perifascicular muscle fiber atrophy was seen (C). Immunohistochemical staining for MHC class I antigens showed intense labeling of the sarcolemma of all fibers and internal labeling of perifascicular atrophic fibers (D). *Bars* A-D 100 μm. A-C, Hematoxylin and Eosin staining; D, immunohistochemical staining for MHC class I antigens.**

is frequently associated with ILD (2). Anti-Jo-1 antibody was reported in 20-30% of patients with PM/DM. ILD was more common than myositis in the early phase of disease and seemed to be one predictor of outcomes. The onset of weakness in patients with anti-Jo-1 antibody frequently occurs between the months of February and July (8). In contrast, anti-SRP antibody is clinically associated with pure PM and is found in 4-6% of patients with PM/DM (1, 3), although three patients with DM were reported among 23 Japanese patients with myositis associated with anti-SRP antibody (9). Patients with anti-SRP antibody most often present with severe muscle involvement characterized by rapidly developing proximal weakness, culminating in severe disability; the response to steroid therapy is often poor. Peculiar histopathological features include prominent muscle fiber necrosis without clinically significant inflammatory cell infiltration.

The present patient's condition was characterized by the coexistence of anti-Jo-1 antibody and anti-SRP antibody. Because the coexistence of these MSAs is associated with the clinical features of both antibodies, interacting in a complex fashion, affected patients may show more severe signs and symptoms. Another characteristic of our patient was the presence of massive pleural effusion associated with ILD. Although lung involvement is often found in patients with PM/DM, massive pleural effusion is very rare (10). The pathomechanism of the massive pleural effusion is unknown, but in this case it may have involved the exacerbation of pleural inflammation in association with pleural microvasculopathy in DM.

In conclusion, our findings strongly suggest that the coexistence of anti-Jo-1 and anti-SRP antibodies may lead to more severe clinical symptoms, including massive pleural effusion, thus expanding the clinical spectrum of idiopathic inflammatory myopathy. However, further clinical and pathological studies of similar cases are needed to establish firm conclusions.

The authors state that they have no Conflict of Interest (COI).

Contributions: K. Sugie was responsible for the overall study design, participated in the organization, planning, and coordination of the study, and wrote the manuscript. Y Tonomura and S Ueno contributed to running the study and analyzed and interpreted the data.

References

1. Targoff IN. Autoantibodies and their significance in myositis. Curr